Trabajo Fin de Máster

Máster Universitario en Diseño Avanzado en Ingeniería Mecánica

Analysis and Design of the Central Stack for the SMART Tokamak

Author: Jorge Segado Fernández

Tutor: Juan Manuel Ayllón Guerola

Dpto. Ingeniería Mecánica y Fabricación
Escuela Técnica Superior de Ingeniería
Universidad de Sevilla

Sevilla, 2022

Trabajo Fin de Máster
Máster Universitario en Diseño Avanzado en Ingeniería Mecánica

Analysis and Design of the Central Stack for the SMART Tokamak

Autor:
Jorge Segado Fernández

Tutor:
Juan Manuel Ayllón Guerola
Profesor Ayudante Doctor Interino

Dpto. de Ingeniería Mecánica y Fabricación
Escuela Técnica Superior de Ingeniería
Universidad de Sevilla
Sevilla, 2022

Trabajo Fin de Master: Analysis and Design of the Central Stack for the SMART Tokamak

Autor: Jorge Segado Fernández

Tutor: Juan Manuel Ayllón Guerola

El tribunal nombrado para juzgar el TFM arriba indicado, compuesto por los siguientes miembros:

Presidente:

Vocales:

Secretario:

Acuerdan otorgarle la calificación de:

Sevilla, 2022

El Secretario del Tribunal

A mi familia

Agradecimientos

Agradecer a mis padres y hermanos, la ayuda y apoyo que me han dado siempre y que me siguen dando, comprendiendo en todo momento el esfuerzo dedicado a mi trabajo, que en muchos casos supone ausencias.

También, agradecer a Juanma, tanto como mentor como amigo, el apoyo que me ha dado para formarme como ingeniero e investigador en todos estos años que llevamos colaborando.

Por último agradecer al grupo PSFT, dirigido por Manolo y Eli, la gran oportunidad que me están dando para participar en un proyecto tan interesante y apasionante como es la construcción del tokamak SMART. También a todos los compañeros del grupo, los cuales son amigos y, en particular, a Javier García por las interminables e incontables discusiones tanto técnicas como personales.

Jorge Segado Fernández

Sevilla, 2022

Resumen

El tokamak SMART (Tokamak de baja relación de aspecto o '*SMall Aspect Ratio Tokamak*') es un nuevo tokamak esférico que está siendo construido en la universidad de Sevilla y pretende estudiar plasmas con triangularidad negativa vs positiva y por primera vez en un tokamak esférico. La operación de SMART va a cubrir tres fases con a campo magnético toroidal $B\phi \leq$ 1 T, corriente inducida de plasma hasta Ip= 500 kA y longitud de pulso de hasta 500 ms, para un plasma con R = 0.4 m, a = 0.25 m y una amplia variedad de configuraciones (ratio de aspecto, 1.4 < R/a < 3, elongación, $\kappa \leq$ 3, y triangularidad, -0.6 $\leq \delta \leq$ 0.6). El sistema magnético del tokamak está compuesto por 12 bobinas de campo magnético toroidal (TFC), 8 bobinas de campo magnético poloidal (PFC) y un solenoide central (CS). Con estas condiciones de operación, el diseño de la columna central, que es un componente crítico en la mayoría de tokamaks esférico debido a la limitación de espacio, presenta importantes retos. La columna central del tokamak SMART se ha diseñado para operar hasta los valores de fase 2 y contiene las barras internas de las TFC, que están rodeadas por el CS, dos anillos de soporte, una barra central y un pedestal. Para alcanzar los parámetros de esta fase ($B\phi$ = 0.3 T con corriente de plasma inducida Ip de hasta 200 kA), las altas corrientes eléctricas necesarias, combinadas con la baja relación de aspecto de la máquina implican grandes fuerzas en los conductores que son un reto desde el punto de vista de la ingeniería. Las cargas esperadas en la columna central son 1.5 MN de fuerza centradora y 6 kNm de torque. Este trabajo describe el diseño de la columna central y la validación mecánica con un análisis de elementos finitos. Uniendo un estudio electromagnético con uno mecánico, la habilidad de la columna central para alcanzar los requerimientos físicos de la máquina hasta fase 2 es asegurada.

Palabras clave: **SMART, Tokamak, Esférico, Columna Central, Fuerza Centradora, Torque**

Abstract

The SMall Aspect Ratio Tokamak (SMART) is a new spherical machine that is currently under construction at the University of Seville aimed at exploring Negative vs Positive Triangularity prospects in Spherical Tokamaks. The operation of SMART will cover three phases, with toroidal fields $B\phi \leq 1$ T, inductive plasma currents up to $Ip = 500$ kA and a pulse length up to 500 ms, for a plasma with $R = 0.4$ m, $a = 0.25$ m and a wide range of shaping configurations (aspect ratio, $1.4 < R/a < 3$, elongation, $\kappa \leq 3$, and triangularity, $-0.6 \leq \delta \leq 0.6$). The magnet system of the tokamak is composed by 12 Toroidal Field Coils (TFC), 8 Poloidal Field (PF) coils and a Central Solenoid (CS). With such operating conditions, the design of the central stack, usually a critical part in Spherical Tokamaks (ST) due to space limitations, presents notable challenges. The current SMART central stack has been designed to operate up to phase 2 and it comprises the inner legs of the TFC, surrounded by the CS, two support rings, a central pole and a pedestal. To achieve the parameters of this phase ($B\phi = 0.2$ T with inductive Ip up to 200 kA), the high currents needed, combined with the low aspect ratio of the machine lead to high forces on the conductors that represent an engineering challenge. The loads expected in the central stack are 1.5 MN of centering force and 6 kNm of twisting torque. This work describes the design of the central stack and its mechanical validation with a multiphysics finite element assessment. By coupling an electromagnetic with a mechanical assessment, the ability of the central stack to meet the physics requirements of SMART phase 2 is ensured.

Keywords: **SMART, Tokamak, Spherical, Central-Stack, Centering-Force, Twisting-Torque**

Index

TABLES INDEX

FIGURES INDEX

1 INTRODUCTION

The energy generation represents one of the most important problem the humanity is currently facing. The principal factors of this problem are the global warming and the increasing energy demands. The first one provoked by the extensive use of fossil fuels for the energy production, currently being more than the 80% [2]. The second one because the expected increase of energy demand cannot be met with the supply means we already have. This increasing is mainly due to the population growth and the decarbonization of carbon-emitter sector with greener technologies but with much intensive energy consumption.

The energy demand is a direct indicator of the societies development and the increasing of population. Considering the current energy demand growth ratio, by 2050, the global consumption will double [3]. While the developed countries are expected to maintain or even reduce their energy demands during the next decades, China will be increasing its demand and the emerging economies are the one with the more important role in this long-term problem. A strong growth in India, Southeast Asian countries or Africa, are foreseen to strongly increase their energy demand.

As stated before, the combustion of fossil fuels emits greenhouse gases that get trapped in the atmosphere leading to the global temperature increase. Due to their low prices and general availability, the energy sector still now relies mainly on them. However, some international events, like the Ukraine war, are showing the risk for a country of relying mainly in external energy suppliers [4]. Moreover, with the current energy demand growth, the reservoir of fossil fuels is expected to be exhausted by 50-100 years. Nonetheless, the climate change is imposing a much tighter schedule for the change of the energy supply with fossil fuels. It is estimated that to keep the average global temperature rise below one and a half degrees Celsius by 2050, 65-80% of the fossil fuels reserves must be left untouched [5].

This context demands a change in the energy production in a hurry. Being both problems very severe, the climate change is getting more attraction, considered in [6] as the most relevant problem the society will have to face during this century. The fulfilment of the next milestones is presented as the guide to avoid a climate disaster:

- Net zero green-house gas emissions by 2050
- Deploy faster and smarter the clean energy supplies already available (i.e. wind, solar, hydro)
- Some breakthrough technologies are needed to complement the latter and fulfil the objective.

The renewables sources are good tools, but not enough for the whole energy frame. The irregularity of their generation, being very localized geographically, very demanding of land or limited in terms of capacity are just a few drawbacks. The hydro-power, currently the main renewable energy source is almost fully exploited. With all these existing technologies, it is expected that at most 60% of carbon emissions can be neutralize. For the rest 40%, there are several proposals based on expected technological breakthroughs:

- **Carbon capture:** this technology aims to capture the carbon dioxide form the air or directly from the emitting processes and storage it underground. It represents a transient help for the process.
- **Hydrogen:** this is an energy storage solution rather than energy source itself. Long-distance transport, freight, shipping, or heavy industry emissions could be solved with hydrogen [7]. However, it presents several drawbacks related with production (very energy-demanding), storage and transport (highly flammability and its tendency to escape from tanks) [8].
- **Nuclear fission:** this mature technology is very interesting for the net-zero emission objective. It solves

many problems of the renewables (power density, delocalized). However, it produces long-lived radioactive waste, the public opinion is very negative with it and is low attractive to the investors due to the high normative associated and the massive previous investment needed to operate it (enormous power plants). New approaches, like the small modular reactors seem very appealing for the proliferation of this technology [9].

- **Nuclear fusion:** this technology is considered as the holy grail of energy generation. It has the same benefits of nuclear fission reducing its drawbacks, since the nuclear wastes are much less risky because of lower quantity and short-lived by-products. Moreover, the fuel is hydrogen that is abundant and very few is needed to harvest huge amount of energy. However, its technical complexity has delayed its commercial deployment several decades. The feasibility of the technology is expected to be demonstrated within the next decade.

Within this framework, this document presents the design of central core of the SMall Aspect Ratio Tokamak (SMART), which is being commissioned at the University of Seville by the Plasma Science and Fusion Technology (PSFT) group. Hereinafter, the nuclear fusion will be described along with the tokamak concept, focusing on SMART. Finally, the motivation of the work and its main goals will also be presented.

1.1 Nuclear Fusion

Nuclear fusion is a physical process that occurred between particles and can yield huge amounts of energy, by joining the nuclei of light atoms to form heavier ones. The difference between the reactants and products masses, following the Einstein equation $E = m \cdot c^2$, is converted in energy. As shown in Figure 1, the joining of separated nucleons (protons and neutrons), create a nucleus with less mass than the separated particles. This difference is converted into energy, the binding energy.

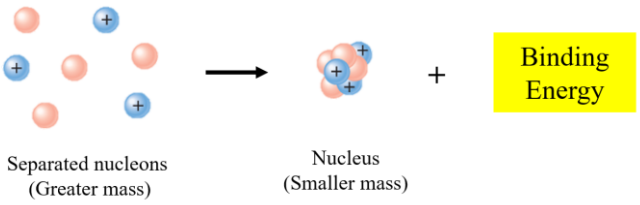

Figure 1: Fusion reaction scheme. The reaction product is a nucleus with smaller mass and the binding energy. Reprinted from: [1].

The strong nuclear force, that joins the separated nucleons, generates a more stable state in the particle and this stability releases energy. The Figure 2 shows the binding energy of different elements, the most stable element is the Fe^{56}, with the highest binding energy. The nuclear fission is based on splitting heavier element to create lighter ones, releasing the binding energy and fusion is the opposite process. As can be seen, the difference of binding energy between lighter elements is much more aggressive than with heavier ones, showing the great potential of nuclear fusion for energy releasing.

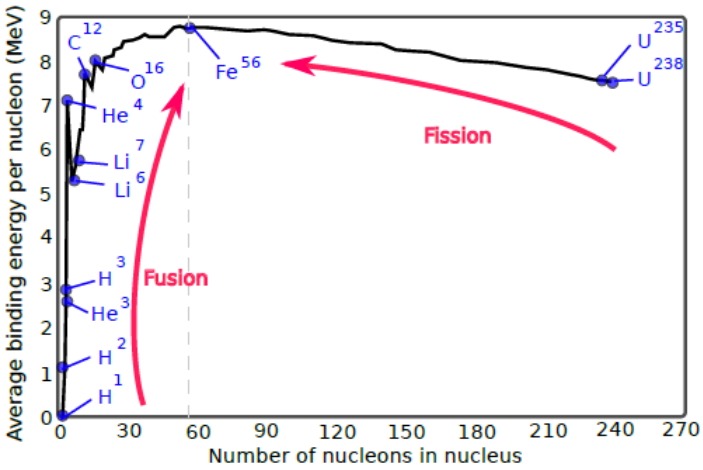

Figure 2: Diagram of binding energy for different elements. Reprinted from: [10].

Although the fission reactions release less energy, achieving and controlling them is technically far easier than nuclear fusion. In fact, that is the reason of the dangerous of nuclear fission and the toughness but safety of nuclear fusion. While the former is based on a chain reaction that can become uncontrollable, the latter has strong barriers that make its achievement quite complex and inherently safe.

In order to obtain the fusion reaction between two positive nuclei, the repulsive Coulomb force must be overcome up to the point in which the strong nuclear force is enough to fuse both nuclei. To overcome the Coulomb force, the nuclei must have very high energy (equivalent to say very high temperature). This energy depends on the elements to fuse, and the most efficient reaction is between two hydrogen isotopes, the Deuterium (D or ${}_1^2H$) and tritium (T or ${}_1^3H$) [10]. The products of this reaction, are one neutron (${}_0^1n$) and one Helium nucleus (${}_2^4He$), both very energetic:

$$D + T \rightarrow {}_2^4He\ (3.52\ MeV) + {}_0^1n\ (14.06\ MeV)$$

In fusion power plant, the products of this reaction will generate heat, that will be used to boil water and produce energy with steam turbines. However, when fusion reactions are attempted, not every energized nucleus fuse, and only those with the right conditions achieve it and release energy. The efficiency of the process is measured with the Lawson criterion, that measures the ratio between the energy being generated by the fusion reactions and the energy losses to achieve them. In a fusion power plant, this ratio must be higher than 1 (in normalized terms) for the process to be self-sustained.

The Lawson criterion stablishes a minimum value for the product of the main fuel parameters. The confinement time (time during which the particles are confined), the density and the temperature of the fuel. The temperatures needed by all these reactions are very high (millions of degrees) and the fuel is in the state of plasma (ionized gas). Due to this high temperature, there is no material that can contain the fuel. In order to confine the plasma several approaches exist:

- **Gravitational confinement:** it is based on the use large gravitational fields to compress the fuel and fuse it. It is the method in which the stars are based on, like the Sun. On earth, the low gravity makes this process unachievable.
- **Inertial confinement:** it is based on the compression of the fuel by an array of lasers.
- **Electromagnetic (EM) confinement:** it is based on the use of magnetic fields to confine the plasma, which has electromagnetic properties and interact with them. This approach achieves low pressures but can obtain very high temperatures (~150 million ºC, that is 10 times hotter than the sun).

Both inertial and electromagnetic confinement experiments have been tested on earth achieving very positive results, being very close to produce net energy. However, the technical complexity of the experiments is very high and, so far, no experiment has achieved the yield of net energy. Inertial confinement reached in 2021 the scientific breakeven (self-sustained reaction) but for a very short period of time and without generating net energy [11]. Moreover, this technology has the drawback that it would be very complex to implement in a steady-state power plant. Regarding EM confinement, so far, the JET experiment has achieved a ratio Q=0.6, that is the ratio of output power to input power, and recently has maintained a plasma with 59 MJ during 5 seconds.

The magnetic confinement has been consolidated as the main approach for creating fusion energy due the good results obtained and the lower complexity to implement it in a power plant. It is worth mentioning that, since the D-T reaction generate neutrons, the power plants will be considered as nuclear facilities and, to reduce the complexity of the research, almost all the scientific experiments dedicated to study nuclear fusion only operate plasmas of hydrogen, that do not generate neutrons. Since this work focuses on the design of the central stack of the SMART tokamak, a magnetic confinement experiment, the next section will focus on this approach.

1.2 Magnetic confinement

As stated before, the plasma is an ionized gas and, therefore, has electromagnetic properties. Magnetic confinement experiments take advantage of these properties to confine the charged particles with magnetic fields. This section will characterize the motion of charged particles within magnetic fields and will present one of the most advanced nuclear fusion experiment based on magnetic confinement, the tokamak.

1.2.1 Interaction between charged particles and magnetic fields

In a plasma, the atoms have the positive and negative charges separated in the nucleus (positive) and the electrons

(negative). Without any external perturbance, they move randomly, but when a magnetic field is applied, the particles interact with them. This interaction is known as the Lorentz's force [12]:

$$\vec{F} = q\vec{v}\ x\ \vec{B} \tag{1–1}$$

Where $\vec{F}$ is the force acting on the particle, q the electric charge of the particle, $\vec{v}$ its velocity and $\vec{B}$ the external magnetic field.

Since it is defined by a cross product, the force is perpendicular to the plane generated by $\vec{v}$ and $\vec{B}$. Figure 3 shows the interaction in a schematic view. As can be seen, the parallel velocity to the field does not interact, but the perpendicular does, and create an helicoidal trajectory around the magnetic field lines.

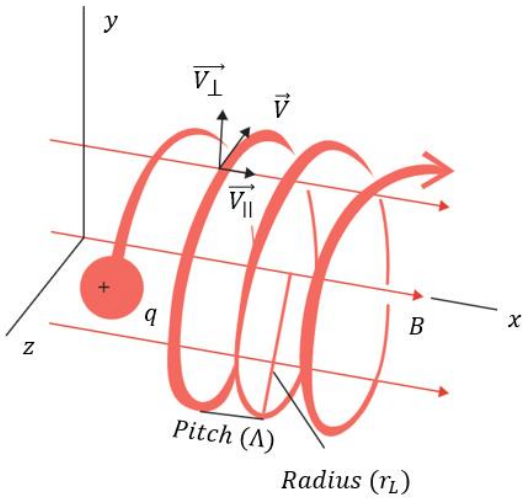

Figure 3: Interaction generated between charge particles immersed in a magnetic field. Reprinted from: [13].

Magnetic confinement experiments use this basic principle to confine the particles and keep them away from the walls of the container. The straightforward arrangement is a linear magnetic field that confined them, but in the ends of the bottle, the particles would scape and it would be very inefficient. A solution presented to this problem was bending the bottle to create a toroidal container. The toroidal field lines would confine the particle avoiding the previous problem with the bottle ends. However, this configuration had other problems associated. The main one is that the toroidal magnetic field is stronger in the inner radius than in the outer one, this tends to separate the positive from the negative particles, creating an electric field, leading to an unstable state that concludes with the particles hitting the walls [14].

To solve the problem of the electric drift of the plasma particles, it was proposed the use of helicoidal magnetic field lines.

Figure 4: Helicoidal magnetic field lines toroidally arranged. Reprinted from: [15].

The main concepts based on the helicoidal magnetic field lines for plasma confinement are the Stellarator and the Tokamak. The Figure 5 represents the basic configuration of both concepts. The main different between them, apart from the coil shape (grey elements) are the way in which they create the helicoidal magnetic field.

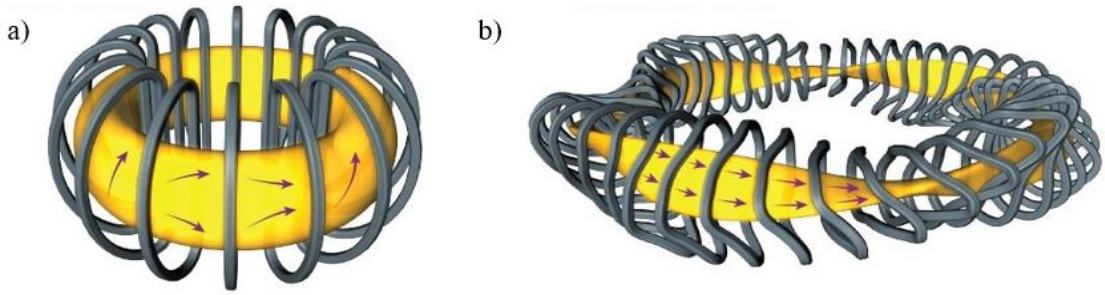

Figure 5: a) the Tokamak configuration; b) the Stellarator configuration. Reprinted from: [15].

The Tokamak creates the helicoidal magnetic field by combining the field generated by two set of coils. The toroidal component is created by one set of coils and the poloidal component is created inducing a current in the plasma. The superposition of both fields composes the helicoidal magnetic field needed. Instead, the Stellarator creates the helicoidal magnetic field with a unique set of coils with a complex and particular geometry. This is the most important difference between both concepts. The tokamak has a simpler coil geometry, but needs to induce a current in the plasma, which forces the operation to be pulsed. While the stellarator has a much more complex coil geometry, but allows the steady-state operation. The main magnetic confinement experiments currently being exploited are the tokamak JET [16] and the stellarator W7X [17].

Since this work is devoted to the design of the central stack for the SMART tokamak, the next section will focus on the detailed explanation of the tokamak concept.

1.2.2 The tokamak

TOKAMAK is a Russian term (TOroidal'naya KAmeras MAgnitnymi Katushkami) that stands for toroidal chamber with magnetic coils. The concept was developed in the 50's by Russian scientist and, since then, it has been improved through the decades, by building bigger and complex machines. The main components of this type of machine are presented in the Figure 6.

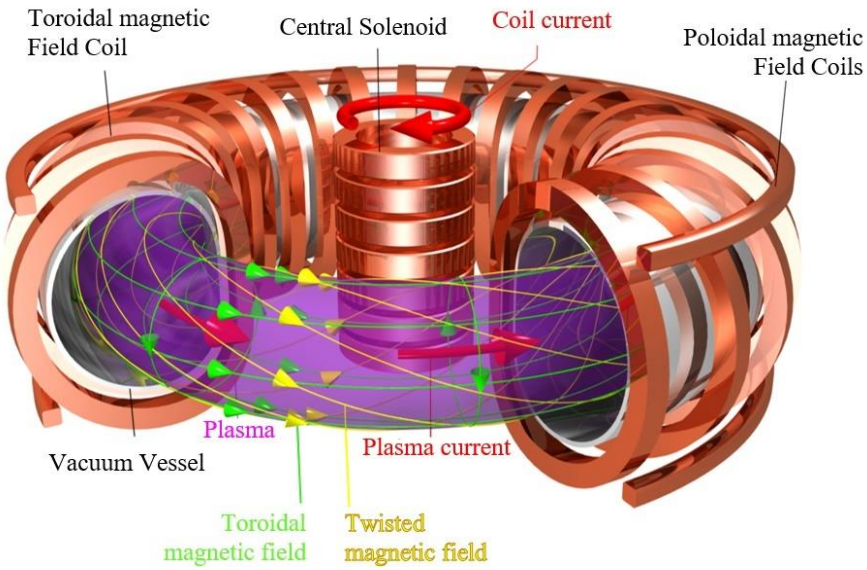

Figure 6: Tokamak basic components basic. Reprinted from [18].

- The Vacuum Vessel (VV) is the component that contains the plasma. However, as stated before, due to the high temperatures of the plasma, they are not in contact with its walls, but the plasma is confined by the magnetic fields. The VV has the main function of creating a clean environment to have plasmas without impurities and allowing the plasma breakdown. To do so it operates in Ultra-High Vacuum (UHV) conditions. It is usually made of non-ferromagnetic Stainless Steel, an important property in this kind of experiments to avoid the creation of huge load due to the interaction with magnetic fields. The inner face of the VV is covered with graphite tiles to protect it from the heat loads than come from the plasma as radiation or during off-normal events.

- The Toroidal Field Coils (TFC) are a set of coils that create the toroidal magnetic field by flowing a poloidal electric current through them.
- The Central Solenoid (CS) acts as a primary of a transformer. By flowing a variable electric current, it induces a current in the plasma (secondary). This plasma current creates a poloidal magnetic field. The addition of the toroidal and poloidal magnetic fields, create the helicoidal magnetic field needed to confine the plasma efficiently.
- The Poloidal Field Coils (PFC) are another set of coils that create a secondary poloidal magnetic field used to shape the plasma and control its position.

These are the main components of a tokamak, but in real experiments there are hundreds of subsystems used to operate the machine at high performance. Some of the most important subsystems included in tokamak facilities are:

- Power supplies to feed the coils with the huge electric currents needed to confine the plasma particles.
- Heating systems to increase the plasma temperature up to the levels require to achieve fusion reactions. Although the plasma current heat the plasma (ohmic heating) other methods are used to complement it. The main heating schemes used are the Electron/Ion Cyclotron Resonance Heating (E/ICRH), based on microwave injection, and the Neutral Beam Injection (NBI), based on the injection of highly energetic particles.
- The divertor that is used to control the extraction of heat from the plasma.
- The vacuum pumps, to reach UHV conditions in the VV.
- Control and diagnostic systems to control the plasma and study its properties.
- Data acquisition systems, to manage the vast quantities of information generated during experiments.

Currently, the most promising project for the realisation of nuclear fusion as an energy source is the tokamak ITER, that is under construction in Cadarache (France). It is expected to start the operation in 2025 and achieve a fusion gain of Q=10 by 2035. However, its main drawbacks are its size and cost. ITER is a huge machine with a total diameter of the VV of almost 20 m that requires tolerances lower than 1 mm in huge components. This high technical complexity is directly associated with the cost. It is estimated a total cost of the project of more than 20 billion euros [19]. These circumstances might lead to the point that, even when the physics and technical problems are solved and demonstrated as a real energy source, its deployment as a commercial alternative, might not be very attractive, due to the high cost and complexity associated.

Nonetheless, there exists other tokamak approaches that try to reduce the size of the machines. One of the main approaches currently being studied is the Spherical Tokamak (ST). This type of tokamak is characterized by the low aspect ratio in comparison with standard tokamaks. The Figure 7 represents the concept of the aspect ratio, that is the ratio between the plasma major and minor radius. In order to consider a tokamak as a Spherical Tokamak, the aspect ratio must be lower than 2.

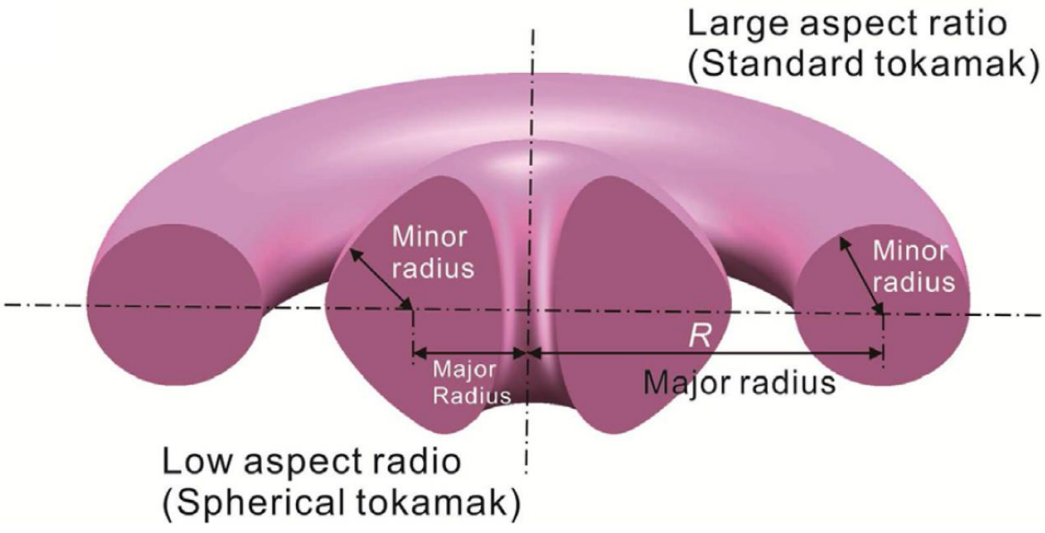

Figure 7: Aspect ratio comparison between spherical and conventional tokamak concepts. Reprinted from [1].

Spherical tokamaks have been consolidated as an interesting alternative to conventional tokamaks due to different reasons. Its main advantage is based on the more efficient use of magnetic fields than in conventional machines. This allows the design of more compact and smaller machines for similar performance [20], [21]. The big cost reduction in the manufacturing of these plants has led to the proliferation of these experimental devices and its proposition as a possible power plant [22], [23]. However, the low aspect ratio implies huge technical hurdles, because the space for the internal parts of the toroidal field coils and the central solenoid is very limited.

1.3 Motivation: the SMART tokamak

This work is devoted to the design of the central column of the SMART tokamak, a spherical tokamak that is being assembled at the University of Seville by the Plasma Science and Fusion Technology (PSFT) group. Its operation is planned to begin by the beginning of 2023.

The SMART operation is structured into three phases, each of them increasing its performance. Table 1 shows the main parameters that will define the operation of the SMART tokamak. They are the plasma current (I_p), the toroidal magnetic field (B_t) and the duration of the experiments (τ). Moreover, the heating power that will be used in each phase is indicated. In phase 1, only ECRH will be used and, from phase 2, both ECRH and NBI will heat the plasma.

Table 1: plasma parameters for the three phases expected for the SMART tokamak [24].

	Phase 1	**Phase 2**	**Phase 3**
$I_p\ (kA)$	100	300	>500
$B_t\ (T)$	0.1	0.3	1
$\tau_{ft}\ (ms)$	100	150	500
$P_{ECRH}\ (kW)$	6 (2.45 GHz)	6 (7.5 GHz)	200
$P_{NBI}\ (MW)$	-	1	1

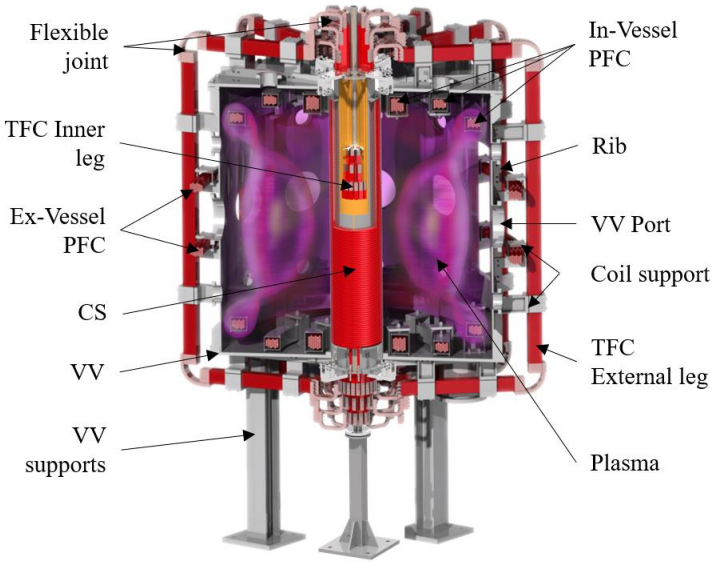

Figure 8: SMART tokamak cross section.

A cross section render of the SMART tokamak is shown in Figure 8. Its main components and the plasma are pointed out and a brief description is presented next:

- Toroidal Field Coils (TFC): the SMART tokamak has 12 TFC, each one formed by four turns of copper bars. The complete TFC is a 48 turns coil (4x12). In turn, each turn of the TFC is formed by the inner and external leg. Since the external leg is attached to the Vacuum Vessel (VV), to avoid the generation stresses in the coils due to the differential thermal expansion, flexible joints have been included to perform the electrical connection decoupling mechanical effects.
- Central solenoid (CS): the central solenoid is a cylindrical coil wrapped around the TFC inner legs in 2 layers, 230 turns arrangement.

- Poloidal Field Coils (PFC): SMART will have 4 pair of PFC. One pair ex-vessel, at atmospheric pressure and three pair in-vessel, in UHV conditions. The in-vessel coils are inside a vacuum casing that protect them from the plasma. The casing is fixed to the VV by flexible lamellae-based supports that can deform to avoid stresses in the coils during differential thermal expansion events.
- Vacuum Vessel (VV): the VV is a cylindrical container made of Stainless Steel 316L (with non-magnetic properties) with an outer and inner wall, 8 mm and 3 mm thickness respectively, creating a toroidal cavity with a rectangular cross-section. The cylinder is closed in the upper and lower sides by two 18 mm thickness lids. To reinforce the walls and lids, the VV incorporates 15 mm thickness ribs every 30º. To allow internal access to the VV, several sets of ports have been included. 2 big rectangular ports have been included in the outer wall for maintenance purposes and to install a Neutral Beam Injection system. 14 ConFlat (CF) 250 DN and 32 CF 100 DN circular ports are included in the outer wall and the lids to include diagnostics, viewports and electrical connections to the in-vessel coils.

Since this work will focus on the design of the central stack of the tokamak, its definition is worth before continuing with the explanation. The Figure 9 shows the same cross-section of the SMART tokamak presented before with the central stack highlighted. The central stack is an independent component of the vessel formed mainly by the TFC inner legs and the Central Solenoid. Its 800 kg weight is supported by a pedestal, to release it from the VV.

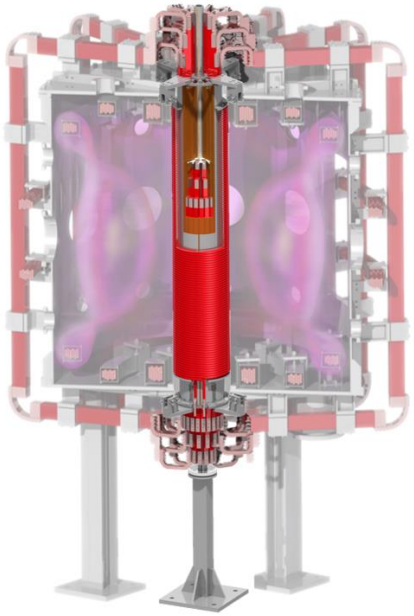

Figure 9: SMART cross-section with the Central Stack highlighted.

1.4 Objectives and Scope

The main objectives of this work are:

- Design the central stack of the SMART tokamak
- Obtain the electromagnetic loads that will affect the central stack during the tokamak operation up to phase 2 performance.
- Verify the structural integrity of the SMART central stack to ensure its safe operation up phase 2. For Phase 3 a new central stack will be designed.

The document will be divided into five chapters. The chapter 2 will define the hurdles associated to the design of the central stack and the SMART central stack. The chapter 3 will present the Electromagnetic assessment of the system based on the finite element method. The chapter 4 will present the structural verification of the system to ensure the safe operation of the tokamak up to phase 2. Finally, the chapter 5 will summarize the work presenting the conclusions and the future work.

2 PROBLEM DEFINITION & SMART CENTRAL STACK

This chapter will present the main concerns associated with the mechanical design in tokamaks and, finally, the design of the SMART central stack. In tokamaks, the mechanical design is directly associated with the electromagnetic loads. First a comprehensive explanation of the main electromagnetic loads presented in tokamaks will be presented. Afterwards, the mechanical design of the SMART tokamak will be presented in detail. The design decisions made based on the reaction of the main electromagnetic loads will be highlighted.

2.1 Electromagnetic Loads in Tokamaks

As presented in the introduction, the Lorentz's law explains the interaction between charged particles in motion and magnetic fields. In tokamaks, the magnetic fields are generated by electric current flowing in coils and these currents, are electric particles (electrons) flowing. Therefore, the interaction between the electric currents and the magnetic fields creates mechanical forces in the conductors. Since the magnetic fields needed in these machines are huge, the current needed too and, therefore, the forces generated in the coils are very relevant in the mechanical design.

When electromagnetic load in conductors have to be studied, the Eq. 1-1 is directly modified to the Eq. 2-1, considering that an electric current is, at the end, a set of charged particles in motion.

$$\vec{F} = \vec{I} ds \; x \; \vec{B} \qquad \textbf{(2–1)}$$

Where $\vec{F}$ is the force acting on the element with current $\vec{I}$ of ds length and $\vec{B}$ is the magnetic field.

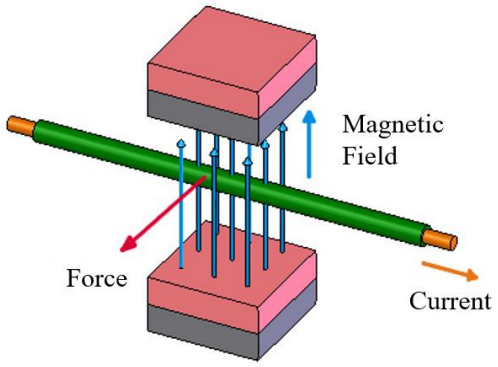

Figure 10: Scheme of the interaction between magnetic field and an electric current, creating a force in the conductor. Reprinted from: [25].

The Figure 10 shows a simple representation of the Lorentz force in a conductor that is immerse in a magnetic field. As can be seen, the force acts in the normal direction to the plane generated by the current and the magnetic field. This simple scheme is enough to understand the origin and predict the direction of the loads appearing in the tokamak coils during their operation. However, the complex set of coils of a tokamak, generates multiple set of interactions, leading to different kind of EM forces. These EM forces can be primarily divided in two big

groups. The first group of loads are generated due to the interaction between the coil current with the magnetic field generated by this same coil. This load is called In Plane Load (IPL). The second group of loads are generated by the interaction between the current of a coil with the magnetic field generated by all the other coils. This kind of load is called Out of Plane Load (OPL).

2.1.1 In Plane Loads

These loads are generated by the interaction between the current flowing in a coil and the magnetic field generated by itself. Attending to the Figure 11, a circular coil generates a force that is bigger in the inner side than in the outer side. This is due to the fact that the magnetic field is stronger inside than outside the coil. This differential magnetic force works as a pressure in a vessel, trying to expand the coil outwards. This magnetic pressure depends on the coil configuration. While in a circular coil, the analogy with a pressurized vessel is direct, in a toroidal coil is not.

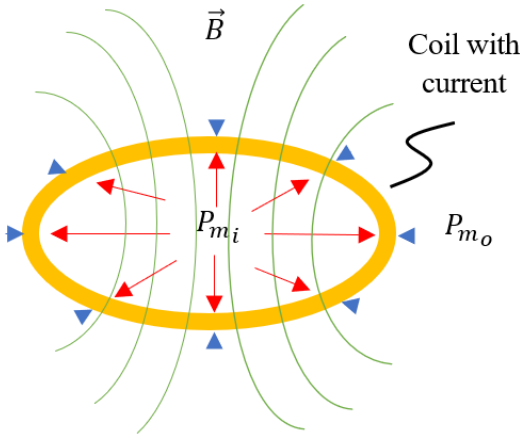

Figure 11: Scheme of the magnetic field generated by a coil with current. The interaction of current and field generates forces, that are bigger inside the coil (Pmi) than outside (Pmo).

To explain the different in plane loads in a tokamak, the SMART magnetic system will be used as reference. Figure 12 shows the magnetic system of the tokamak, differentiating with colors the different kind of coils.

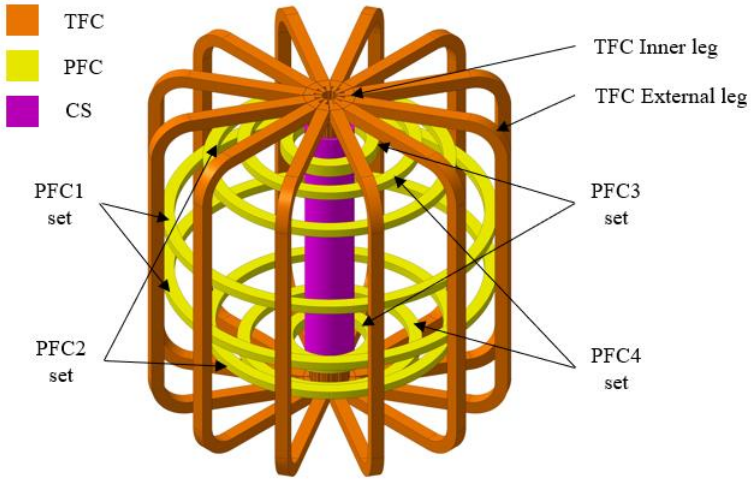

Figure 12: SMART magnetic system

- **Thin cylindrical coil:** the Poloidal Field Coils (PFC) are this kind of coils. The explanation of the Figure 11 is of direct application in this case. The magnetic pressure tends to expand radially outwards the coil.
- **Thick cylindrical coil:** the central solenoid is this kind of coil and has associated two kinds of IPL. The main one is the same as in thin cylindrical coils, a radial pressure than tends to expand the solenoid outwards. However, due to the bend of the magnetic field at the coil ends, a compressive load is generated too in the solenoid. It is worth mentioning that this load is not 'in the plane' of the coil, but has been considered here, because is caused by the interaction of the coil current with its own field.

- **Toroidal coil:** as in a circular coil, the toroidal coil generates a magnetic pressure inside its volume that leads to a radially outward pressure load. However, in a toroidal coil, the magnetic field decays with the radius exponentially. Therefore, the load in the inner region of the TFC is much stronger than in the outer one. Figure 13 shows in a) the toroidal magnetic field strength and, as can be seen, it decays with the radius. In b) is shown the EM load generated in the coil, that it also decays exponentially with the radius, following the magnetic field strength, while the electric current is constant in all the coil.

  In the case of SMART, since the coil is rectangular, the load can be divided in vertical load, that is self-equilibrated and horizontal force. Due to the different radial positions of the inner and outer legs of the TFC, the loads are much bigger in the inner leg that in the outer one. That is known as the centering force ($F_{centering}=F_{in}-F_{out}$), that compresses the TFC to the center of the tokamak.

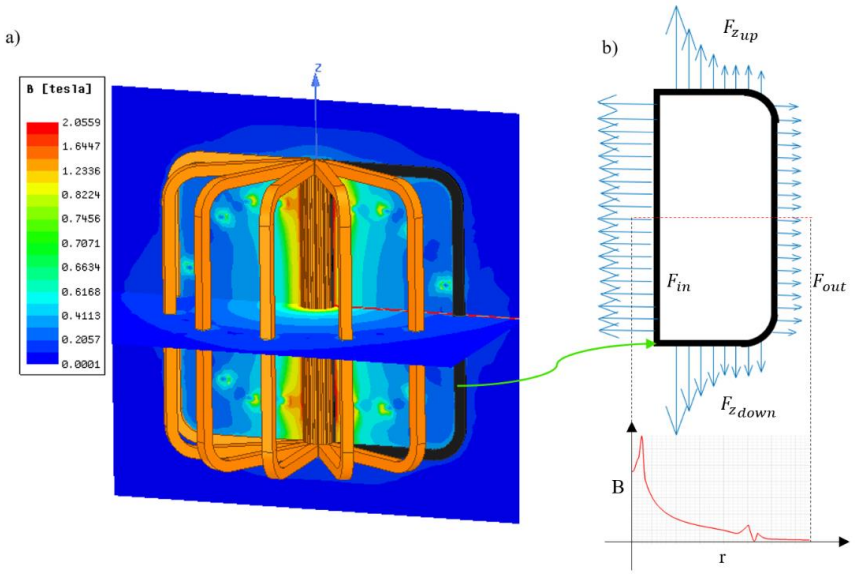

Figure 13: a) Toroidal magnetic field strength of the SMART tokamak; b) IPL generated in a single TFC.

2.1.2 Out of Plane Loads

The Out of Plane Loads (OPL) appear in the normal direction of the coil plane and due to the interaction between the coil current and the external magnetic fields. In a tokamak, they appear due to the interaction of the different coil systems. The main types of OPL are:

- **Interaction between two circular coils:** this interaction is similar to the one generated between two close magnets. The Figure 14 shows the forces generated in parallel circular coils depending on the direction of the electric current on them. When the direction of the currents is the same (north and south poles of the magnets together) the force is attractive. When the direction of the currents is the opposite (same poles together), the force is repulsive.

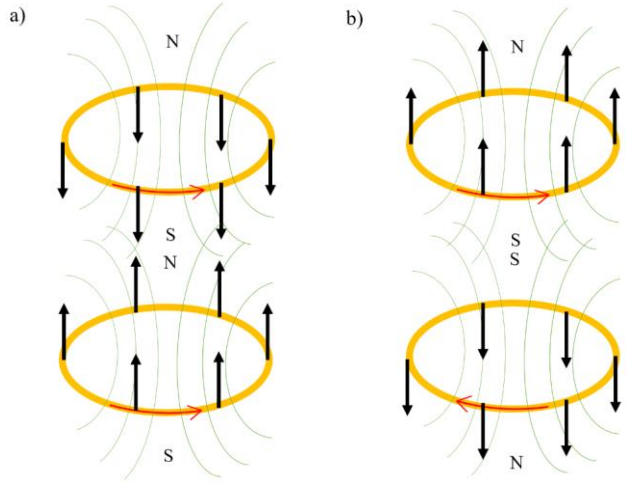

Figure 14: interaction of circular coils depending on their current direction. a) attraction – same

direction; b) repulsion – opposite direction.

- **Interaction between toroidal and circular coil:** the interaction between the electric current of the TFC and the magnetic field of the PFC and CS creates a force perpendicular to the plane of the TFC. The Figure 15 shows in a) the poloidal magnetic field of the SMART tokamak and in b) the OPL generated in the TFC due to the interaction between its current (red arrow) and the crossing field lines. As can be seen, the bigger loads appear again in the inner leg of the TFC, where the vertical current interact with the bend field lines of the central solenoid, which has the strongest field. This load in all the TFCs generates a torque in the central stack that is self-equilibrated and try to squeeze it.

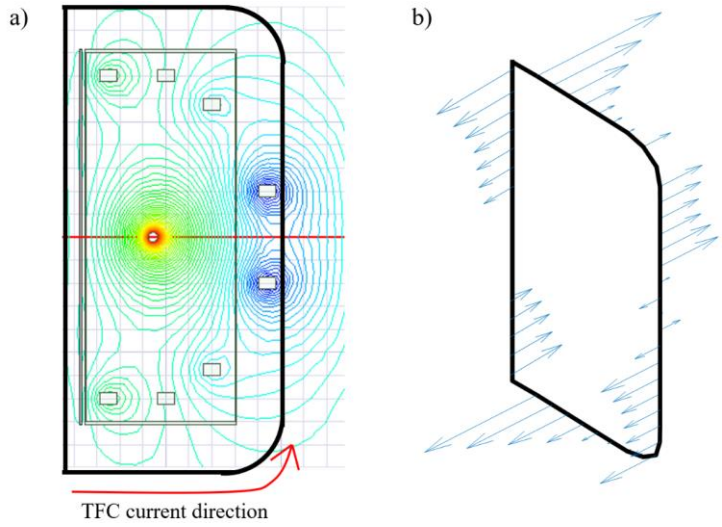

Figure 15: a) SMART poloidal magnetic field; b) OPL generated in the TFC.

In order to focus on the component that will be design throughout this work, the loads that appear in the central stack are summarized in Figure 16. In a) the IPL is shown in both the solenoid and the TFC inner legs. The colored arrows indicate the strength of the force. In the solenoid the bigger force is in the inward part, where the magnetic field is bigger, and the force is radially outward in general. In the TFC inner legs the outer legs have the biggest centering force, since the magnetic field strength is maximum inside the TFC volume, that is closer to the legs of the outer zone. In b) the OPL generated due to the interaction between the TFC inner legs current and the field of the solenoid ends, is represented as a torque composed by the force in all the legs. As will be seen in the next section, the torque is going to be partly reacted by the arms depicted in the figure.

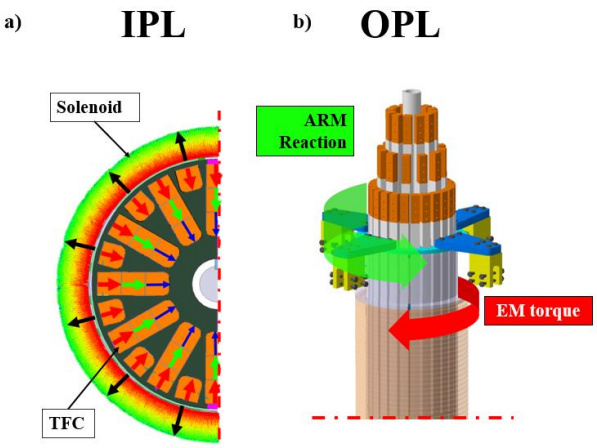

Figure 16: a) IPL; b) OPL in the central stack of the SMART tokamak.

2.2 The SMART Central Stack

The SMART Central Stack (CS) is a component that includes the Toroidal Field Coil (TFC) inner legs and the Solenoid creating an individual component. Its cross section is shown in the Figure 17 where the main dimensions are indicated. The inner diameter of the TFC inner legs is 90 mm and the outer 232 mm (not shown). Between the TFC and the solenoid there is a gap to reduce the tolerance requirements during manufacturing.

The solenoid inner diameter is 240 mm and the outer one 296 mm. The rest of the components are structural support that will be explain later.

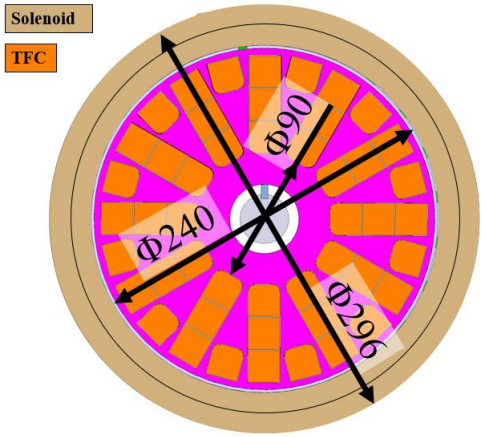

Figure 17: Cross section of the SMART central stack. Main dimensions indicated.

2.2.1 Central Stack Optimization

The configuration of the conductors in the central stack was optimised based on electrical parameters [26] and tries to maximize:

- The TFC inner leg area with square conductors. Usually, in other spherical tokamaks, these legs are wedge-shaped to optimize the space used by the conductor [27], [28], [29]. In SMART, square conductor has been selected to reduce the budget of this component, since the machining of these wedge-shaped bars is quite expensive. By rounding the edges of the inner bars and the central outer bars, the cross-section of the bars was maximized while leaving free space for mechanical support. In total, the central stack is composed by 48 bars with 480 mm^2 of section (21.9 x 21.9 mm). The interesting point of maximizing the cross section of the conductor is that it allows to carry more current while limiting the temperature increase, extending the pulse length for the same temperature limit.
- The solenoid is wrapped around the TFC inner legs to place it in the larger radius possible. This allows the maximization of the flux swing of the solenoid for a given current. The flux swing is the capacity of a coil to generate an inductive voltage during a time. It is measure in V·s or Webers (Wb) and it is obtained following the Eq. 2-2.

$$f_s = A \cdot dB \tag{2–2}$$

  Where f_s is the flux swing, A the cross-sectional area of the coil and dB the differential magnetic field to be integrated in the area. For a cylindrical solenoid, the flux swing is directly obtained as $f_s = A \cdot B$.

  The SMART solenoid has 2 layers of conductor with a total of 230 turns. The conductor cross-section is 105 mm^2 and it can produce the flux swing required to ramp-up the plasma current up to 200 kA and sustain it for 150 ms [24].

The central stack design parameters are shown in the Table 2:

Table 2: Central Stack design limit parameters.

	Design limit
Solenoid max. current (kA)	10
Flux swing (mV·s)	112
TFC current (kA)	16.8
B_t(T)	0.4

With the maximum electric current that the solenoid can flow (10 kA) based on electric and thermal limits, the maximum flux swing achievable is 112 mV·s, a value of the same order that state-of-the-art spherical tokamaks, like Globus-M2, with a maximum flux swing of 150 mV·s [29]. On the other hand, the TFC max current of 16.8 kA, again stablished by electric and thermal limits can generate a toroidal magnetic field in the major radius of the tokamak of 0.4 T. This value is not the maximum achieved in a spherical tokamak, but it is already enough

performance to study first-class plasma physics [30].

2.2.2 Central Stack Mechanical Design

Once the main features of the central stack have been presented, this section will be devoted to present its mechanical design. The central stack is 2.6 m height, 296 mm diameter and 800 kg weight. The weight is independent from the Vacuum Vessel to reduce its supporting requirements. The angular position can be easily adjustable avoiding tight tolerances in the manufacturing. The Figure 18 presents the SMART central stack pointing the main mechanical components that shape it. From the inward parts:

- The **central pole** is a 48 mm external diameter, 7 mm thickness calibrated bar and is the core of the system. It is supported by the **pedestal** that fix the height, but it is adjustable with bolts to calibrate the final position during assembly. The central pole is made of SS316L and the pedestal of SS304. To avoid magnetic flux consumption by the central pole, it is longitudinally cut along its complete length. To give mechanical support in this cut while maintaining the electric break, a **PEEK insert** has been included. The PEEK is a technical polymer with excellent mechanical properties and high vitreous transition temperature (<180ºC).
- The two **torque rings** (up and down) are bolted to the central pole. The TFC inner legs will be inserted in them during assembly. Moreover, they will restrain the legs position during operation when the out of plane loads will generate a torque. The torque rings are made of SS316L.
- To help the positioning during the assembly phase, two **spacer discs** are included too. They are attached to central pole. These are made of epoxy G10 to reduce risk of possible electrical short cuts between the bars and the rings.

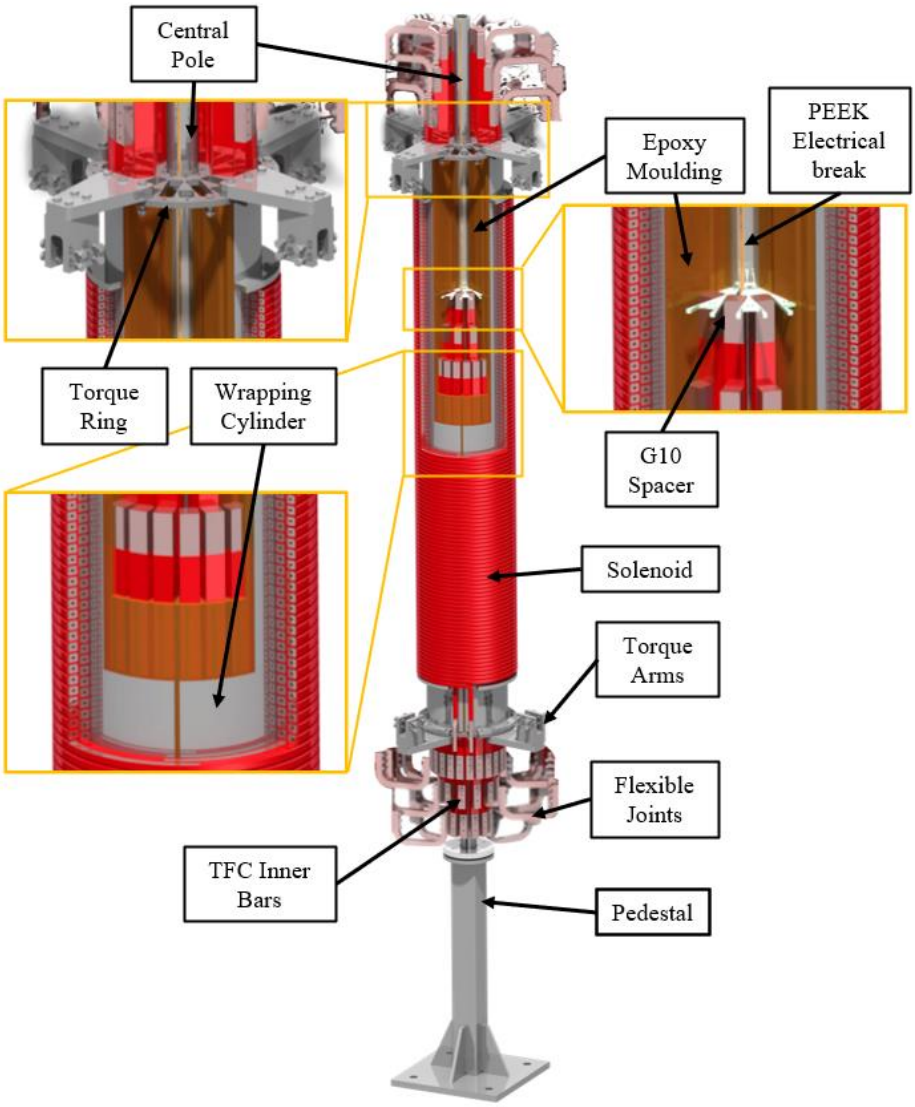

Figure 18: SMART central stack.

- The **48 TFC inner bars** are inserted and guided by the torque and spacer rings. They are Oxygen Free (OF) copper bars with 480 mm^2 of cross section provided by Luvata [31]. The electrical insulation is made with 50 μm of kapton tape and 200 μm of TUFQUIN TFT layer [32]. This insulation gives a total strength of 20 kV while the maximum voltage expected during operation is 2 kV.
- The **solenoid** is wrapped in 230 turns and 2 layers around a 2 mm thickness **wrapping cylinder** made of SS316L. The conductor is again OF copper with 105 mm^2 of cross-section and with a 4 mm diameter hole for cooling provided again by Luvata. The insulation is made by 185 μm of Kapton tape giving 50 kV of insulation strength for a maximum expected operational voltage of 6 kV. The wrapping cylinder is longitudinally cut too to avoid flux consumption.
- The components inside the wrapping cylinder (TFC bars, rings, pole, etc.) will be solidified with **epoxy** (SR1720) [33] to give mechanical stiffness to the assembly.
- Once manufactured and assembled in the Vacuum Vessel (VV) central column (300 mm diameter pipe), the central stack will be angularly positioned with the **torque arms**. These arms will join the torque rings with the VV lid ribs. The join to the ribs will be made with adjustable bolts, reducing the tolerance requirements during the manufacturing. These arms are made of aluminium 7075 T651.
- Finally, the electrical connection between the inner and outer legs of the TFC will be carried out with lamellae flexible joints bolted to each end. These flexible joints are very important to decouple the electrical connection from the mechanical loads (i.e., EM or thermal load). There have been several problems in other spherical tokamaks related with these connections due to excessive stiffness in bolted joints, that led to electrical short-cut after a certain number of experiments [27], [34]. The solution implemented in SMART have been already tested in other machines [35], [29], [36].

Finally, regarding the mechanical design, it is worth mentioning the justification of the main design choices based on the support of the EM loads presented in the Figure 16 (In Plane and Out of Plane Loads):

- The **IPL** is a centering force self-equilibrated by each TFC bars and its opposite. Therefore, it is only needed to include mechanical support between them to allow this compensation between each other without damaging the copper bars. To do so, the central pole is included as a stiff support. To complete the load path between the bars and the central pole, the epoxy is included transmitting the load in the whole area of the bars, avoiding stress concentration points.
- The **OPL** is a torque generated in the upper and lower part of the TFC bars and is self-equilibrated. The epoxy joins all the TFC bars to create a 'composite block' of copper+epoxy. However, the 'fibres' (copper) are not well aligned to withstand torque, being in the torque axis. To reduce the structural requirements to withstand the load, the torque rings are included and joined to the massive vacuum vessel lids (18 mm thickness of SS316) by means of the torque arms. As will be shown in the structural analysis, the 50% of the torque is reacted by the arms and the other 50% by the central stack itself. Moreover, the arms restrain the system in case the upper and lower torque are not perfectly equilibrated, protecting the electrical joints of withstanding it.

2.2.3 Manufacturing status

By September 2022, all the major components of the central stack are manufactured and stored in the Centro Nacional de Aceleradores. The assembly and solidifying with epoxy will be carried out in the MGcompites [37] facility and is planned to start by the beginning of December. The assembly of the central stack in the tokamak vessel is expected for the beginning of 2023. The Figure 19 shows several pictures of the main components of the central stack. The SMART vacuum vessel is also shown.

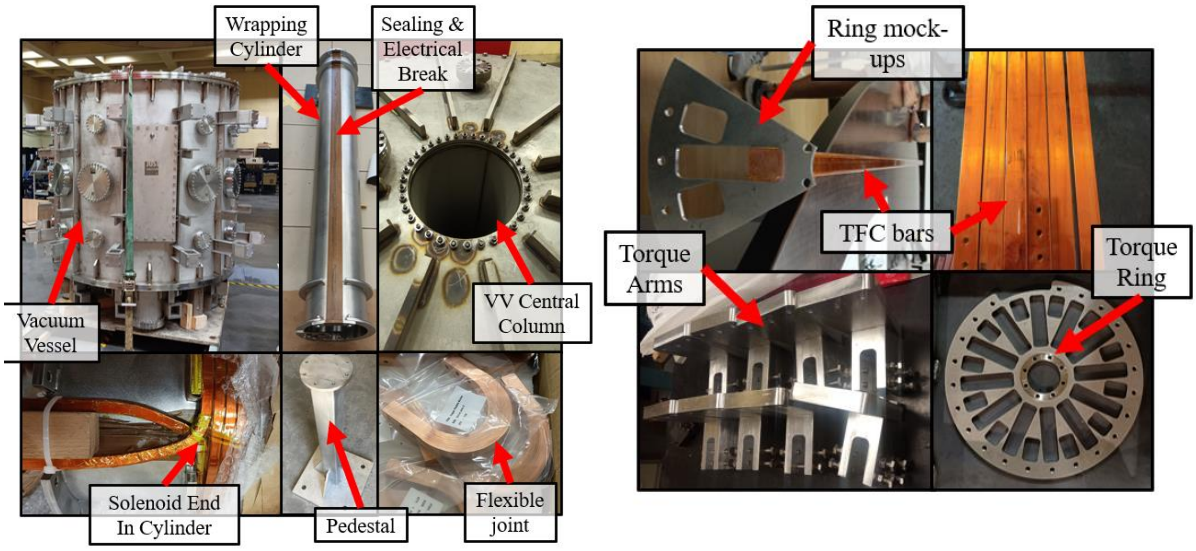

Figure 19: Pictures of the manufacturing status of the central stack components by September 2022.

3 ELECTROMAGNETIC ASSESSMENT

The main loads of the central stack explained in the previous chapter are electromagnetic load. These are generated just by the electric current flowing in the coils used to generate the magnetic fields that confine the plasma particles. While for simple problems the Lorentz Law is directly applicable, when the complexity is increased, it is not possible to calculate the EM loads analytically in an accurate way. As stated in the previous chapters, the magnetic system of a tokamak is quite complex and, therefore, other methods to assess the EM loads are used. The most common one is by using the Finite Element Method (FEM).

This work uses the FEM software ANSYS Maxwell, included in the ANSYS simulation suite. It allows the study of electromagnetic problems by solving the Maxwell's equations within a region of space using the T-Ω formulation [38]. The software generates the mesh automatically based on an adaptive meshing technique which uses tetrahedron elements of 2nd order and 10 nodes. The user can control shortly the mesh, being able to select the mesh size within specified geometries, but the general mesh cannot be controlled in detail. This is due to the fact that the software meshes the geometry of interest and the surrounding region, where the Maxwell equations are solved and then, the resulting mesh is a continuous block. The result convergence is based on energy criteria and the limit stablished for this study is 0.1%. The result of this model is the volumetric EM forces generated in the coils. These forces are then exported to the mechanical FEM model where the structural integrity is studied, as will be presented in the next chapter.

This chapter presents the assessment of the SMART magnetic system in ANSYS Maxwell. First, design scenario for the central stack design will be defined based on the SMART operation. Next, the FEM model generated is presented, attending to the geometry included, the model input and the mesh. Finally, the results of the model, that are the EM loads generated in the coils, are presented.

3.1 Design Scenario

The scenario for the SMART central stack is defined by the currents that each coil has during the experiments. As shown in Figure 12, the SMART magnetic system is formed by 3 set of coils. The TFC has the same current in all the coils and is a constant current during the experiment. However, the solenoid and the poloidal field coils, have different currents and they vary during the experiment for different physics purposes, like the plasma breakdown, the vertical stability or the plasma shaping [39].

As mentioned previously, the central stack presented with this work for the SMART tokamak is designed to ensure the operation up to phase 2 parameters (Table 1). In order to be conservative in the mechanical design and structural verification, the design scenario will be defined with the current limit of the coils imposed by electric and thermal reasons. Therefore, to obtain the design scenario inputs, the currents of the reference scenario of phase 2 [39] will be scaled up to the limit current.

The Figure 20 shows the current waveform of the reference pulse of SMART scaled up to the design limit current (2.5 times). This method has been implemented instead of directly applying the maximum current, because, as can be seen, the current waveforms do not have their maximum at the same time.

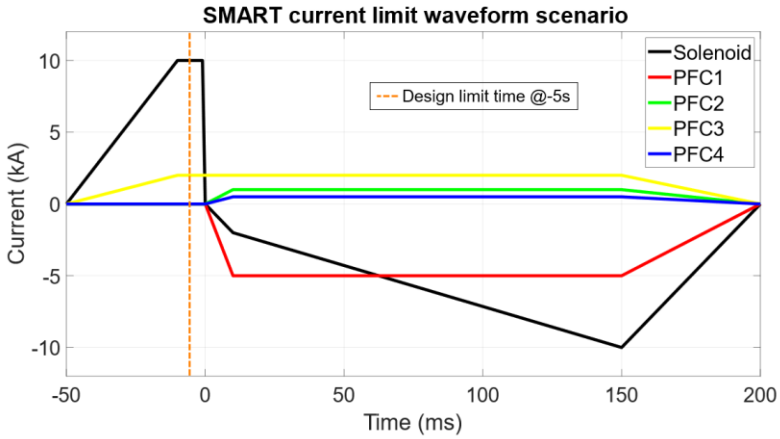

Figure 20: current waveform scaled up in solenoid and poloidal coils for the design limit scenario.

Once the current waveform of the design scenario is defined, an instant will be selected to simplify the analysis, allowing to perform it as an electrostatic model. The difference with a transient model would be important when the current inductance in passive elements is an issue (i.e, structural verification of the vacuum vessel [40]) but in this analysis it is not. This instant will be the point in which the currents in the coils closer to the central stack are maximum. These closest coils are the central solenoid and the PFC set 3 (from Figure 12). The bigger the current in them, the bigger the magnetic field and the bigger the loads generated. The current in the rest of PFC sets, are not relevant for the central stack loads. Therefore, the instant that will be considered for the analysis is at -5 ms, just before the plasma current starts, because at this time, the solenoid and PFC set 3 have their maximum currents and in the same direction, adding their magnetic field strengths.

The current values that will be used as inputs of the FEM model for the EM analysis are summarised in the Table 3 for each set of coils.

Table 3: Electric current input for the EM analysis of the design limit scenario.

	Electric current (kA)
Central Solenoid	10
PFC set 1	0
PFC set 2	0.1
PFC set 3	2
PFC set 4	0
TFC current (kA)	16.8

3.2 Model

This section will explain the model created for the simulation of the SMART central stack in ANSYS Maxwell. The components considered and the mesh will be presented.

From the realistic CAD model presented in previous chapters of the tokamak, the geometry considered for this model is very simplified. The Figure 21 compares the realistic CAD geometry; with hundreds of details, like the bolts or the insultation; with the model considered in the EM FEM model, which only considers the SMART magnetic system with a simplified geometry. For instance, the real solenoid has 230 turns, however, in this model is just a cylinder with the same external geometry than the real one. It is important to clarify that the details are not needed because this model will only be used to obtain the EM load generated, and this is just provoked by the interaction between magnetic fields and electric current. Therefore, the details are not important, and they would only increase the complexity of the model. The TFC is modelled with all the turns because the load will be generated in their bars, that is the objective of this model, but again, the details of the TFC have been simplified to reduce the computational cost of the model.

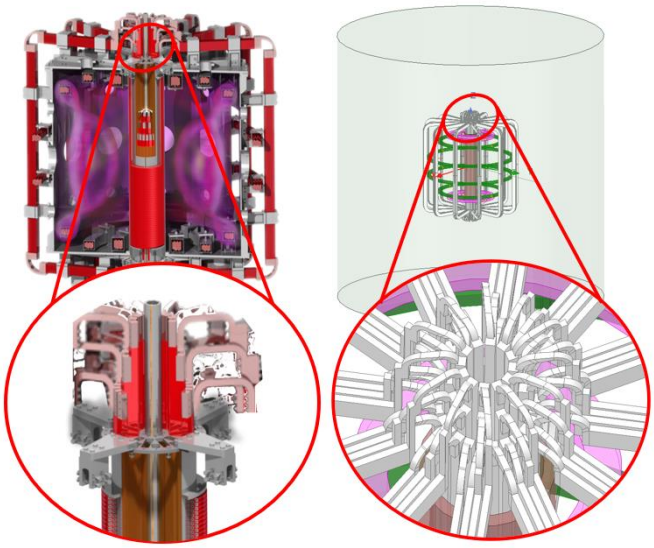

Figure 21: Geometry simplification for the SMART model implemented in ANSYS Maxwell.

From the Figure 21 it is worth mentioning that the green cylinder, surrounding the complete model, is the region where the software will solve the problem (Maxwell's equations). All the volume inside this region will be meshed. Its dimensions are specified with some margins with respect to the model limits to avoid boundary effects near the zone of interest. As already mentioned, the passive elements, such as the vacuum vessel are neglected in the model because the analysis is electrostatic and there will not be electric current induced in them during the assessment.

Regarding the mesh, the model has 1.6 million of elements in total. Being the region the component with more elements (1.2 M). The Figure 22 shows the mesh of one TFC and the solenoid as example of the kind of mesh generated by the software. The solenoid has 20 k elements, each TFC turn around 8 k and the PFC coil around 2 k, being the less refined elements, due to their lower importance for this analysis. As mentioned before, the software generate the mesh by an adaptive iterative method based on an energy criterion. The energy error limit used in this analysis is 0.1% and the software converged after three mesh refinement passes, going form 900 k elements to the final 1.6 M.

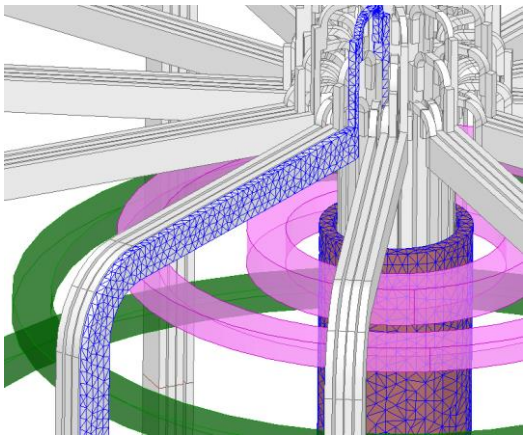

Figure 22: Mesh of one TFC turn and the solenoid.

3.3 Results - EM Loads

Once the model is presented, this section will present the results obtained, that are the EM loads generated in the conductors. First, the magnetic field generated with the input current considered in the design limit scenario is shown in the Figure 23. As can be seen, the maximum strength of the magnetic field is generated in the zone of the central stack, as previously explained. Indeed, just the space between the central solenoid and the TFC inner legs positioned more outward, is the critical zone with a maximum field of 1.5 T. Therefore, this zone will have the maximum loads.

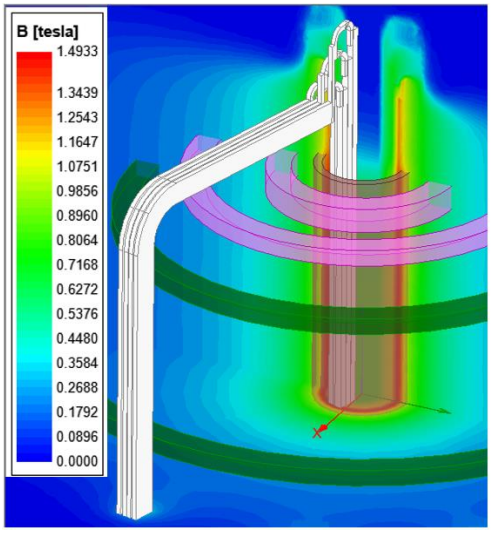

Figure 23: Magnetic field generated during the design limit scenario.

Figure 24 shows the EM force generated in the solenoid during the simulation. In the detail can be seen how in the solenoid ends, the load is almost completely vertical and compressive, while, far from the ends, the load is completely radial, being maximum in the inner face.

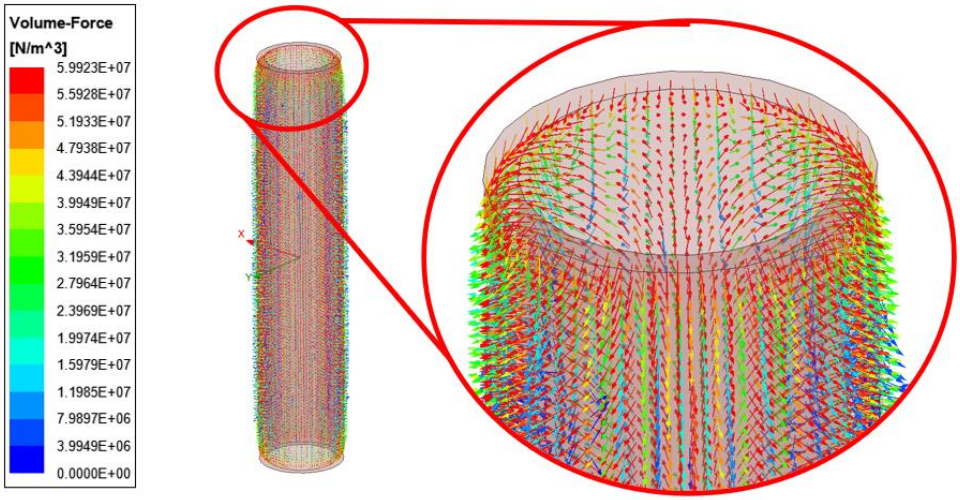

Figure 24: EM force generated in the solenoid during the simulation of the design limit scenario.

Figure 25 shows the EM force generated in one complete TFC (4 turns) during the simulation. In the detail can be seen how the OPL is generated just in the solenoid end. The addition of this OPL in the 48 bars generate the total torque in the central stack. Apart from this zone where the OPL is generated, the rest of the load is in the coil plane (IPL) being radial and outwardly oriented (magnetic pressure). As was explained in the Figure 13, the inner legs are the most loaded parts, since there, the field is maximum and decays exponentially with the radius, as is stated in this image, where the TFC outer legs has IPL several order of magnitude lower than the inner legs. Moreover, as also shown before, from the 4 inner legs of each TFC, the positioned in the outer zone of the central stack, are the most loaded, because are the closest to the maximum magnetic field inside the TFC volume.

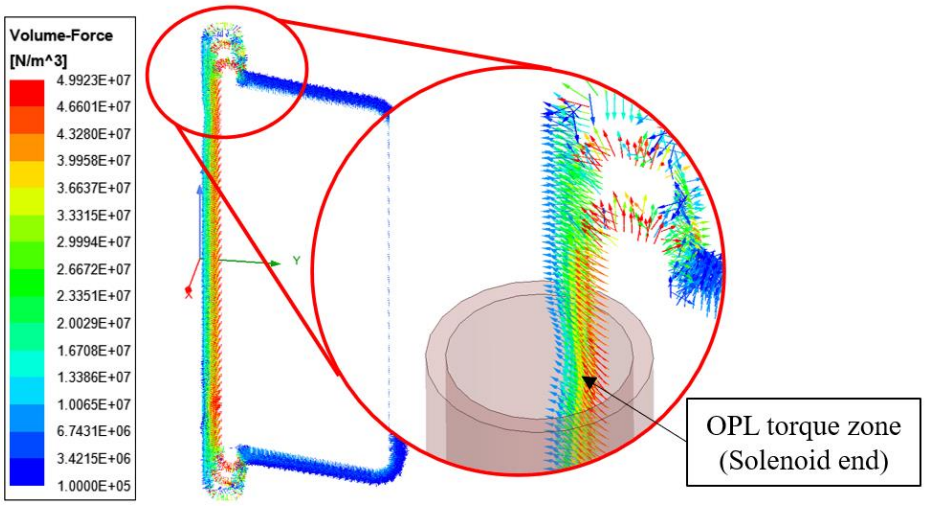

Figure 25: EM force generated in one complete TFC (4 turns) during the simulation of the design limit scenario.

The Table 4 presents the load obtained with the model for the design limit scenario. The load indicated correspond with those qualitatively shown in Figure 16. The centering force exerted by the 48 TFC inner legs is 1.5 MN, the torque generated around the central stack vertical axis, by all the TFC inner legs, is 7.4 kNm. Regarding the solenoid, the outward radial pressure is 1.6 MN, being equivalent to 1.3 MPa of magnetic pressure and the vertical compressive pressure is 120 kN, being equivalent to 2.6 MPa of magnetic pressure.

Table 4: Load obtained for the design scenario with the EM model in ANSYS Maxwell.

	Design limit load
Total TFC IPL [MN]	1.5
Total TFC OPL (torque) [kNm]	7.4
Solenoid radial pressure [MN]	1.6
Solenoid compressive pressure [kN]	120

Once the EM loads in the central stack have been obtained, they will be exported to a mechanical FEM model created in ANSYS Mechanical to verify the structural integrity of the system during the design limit operation. This will be presented in the next chapter.

4 STRUCTURAL ASSESSMENT

Once the EM loads that will be generated in the central stack during the SMART operation have been obtained in the FEM model created in ANSYS Maxwell. The structural verification of the system can be performed. Another FEM model will be used for this task and will be created with the ANSYS Mechanical software, that allows the coupling with the results of the previous EM model.

ANSYS Mechanical is another FEM software integrated in the ANSYS simulation suite dedicated to the study of structural and thermal problems [41]. This software integrates countless types of elements, both of 1st and 2nd order, hex and tet types and for different kinds of analysis. The mesh can be defined in detail by the user. In this work the confidence of the results will be assure by converging their values with an error limit of the 5%.

This chapter presents the structural verification of the SMART central stack to ensure the safe operation of the system up to the tokamak phase 2. First the codes and standards used for the structural verification will be presented along with the SMART design criteria. Afterwards, the FEM model created to study the mechanical behaviour of the system will be explained. Finally, the results of the verification when the EM load is applied to the system will be presented.

4.1 Codes and Standards used for structural verification in nuclear fusion

Since the nuclear fusion is not already an industrial sector, it is not quite regulated. However, the proliferation of huge international projects, like ITER, that involved diverse industries from several continents is contributing to the development of a regulated framework for the design of fusion projects. In particular, ITER has already developed a code for the design of the components that will be located inside the vacuum vessel. It is called the ITER Structural Design Criteria for In-vessel Components (ITER SDC-IC) [42]. It is worth mentioning that this standard has not been developed entirely for the project, but it is based on other codes from several industries. The ASME Boiler & Pressure Vessel Code, section III and VIII and the RCC-MR of the French nuclear industry are the major contributors to the ITER SDC-IC code [43]. Moreover, it includes particular rules and recommendations specific for the environment presented in a tokamak, with huge heat loads and magnetic fields.

The ITER SDC-IC code has been selected as the reference for the SMART design criteria. Although this standard is quite complete, only the important points for the SMART project have been considered, neglecting many of them for being out of the scope of the SMART project (i.e., influence of neutron dose in the material properties).

In summary, for the structural verification of the system, the code has been used to stablish the damage and failure modes and the stress classification.

Regarding the damage modes, they will be classified as Monotonic and Cyclic damages [44]:

- **Monotonic damages** refer to those damages resulting from the application of steadily and regularly loading or a constant loading to the structure. The failures associated to this kind of damage are:
    - Plastic instability.
    - Excessive deformation.
- **Cyclic damages** refer to those damages resulting from the application of loads repeatedly. The failures

associated to this kind of damage are:

- Progressive deformation.
- Fatigue.

Regarding the stress classification, the code divides them in primary, secondary and peak stresses depending on the origin of the stress (i.e., thermal load, mechanical load):

- **Primary stress** (generated by mechanical effects) is any stress created by an imposed loading which has to satisfy the simple laws of equilibrium of external and internal forces and moments. They are not self-limiting stresses. They are load-controlled stresses in the sense that they react the application of mechanical loads.
- **Secondary stress** is any stress created due to the constrain of adjacent components or by self-constraint of the component itself. Usually arise from thermal expansions and are self-limiting stresses. The stresses are self-equilibrated and produced by non-uniform thermal distribution or by the interaction among dissimilar elements. They are displacement-controlled stresses.
- **Peak stress** is the growth of stress provoked by local discontinuities or local thermal stresses.

In turn, the primary stress is divided in membrane, bending and peak stress, depending on their distribution along a path defined in the component studied. This method of stress classification is called linearization. Its objective is to separate the stresses depending on the damage they can produce. In this way, it is allowed the application of different safety factors for each stress, thus, increasing the optimization of the design [45]:

- **Membrane stress** is the average stress along the path specified in the component to linearize the stresses. It is constant along the path. In terms of energy, it is the most demanding stress, since the whole component has this level of stress. If the membrane stress generates the yielding of the material, the structure will not redistribute the load to the surrounding material, because are all at the same level. Therefore, the safety factor related to this stress is the lowest.
- **Bending stress** is a stress component that varies linearly along the path. In comparison with the membrane, with this stress, the whole component is not subjected to the same level of stress, therefore the energy associated is lower and the safety factor can be more relaxed. In case of the material yielding, the stress would be redistributed to the surrounding material, that is less demanded.
- **Peak stress** is the rest of the stress obtained from the difference between the original stress along the path and the sum of membrane and bending (different from the *'peak stress classification'* mentioned before). In this case, the safety factor is the looser, since the stress is very concentrated in a point, and it can be redistributed in the rest of the material in case of yielding.

To clarify the explanation of the stress linearization, the Figure 26 is presented. It represents the stress distribution along the thickness of a component under mechanical loads (red curve). When the stress distribution is linearized, the stress is divided in membrane (orange line), bending (green line) and peak (blue line) stresses. The peak stress varies in each point to complete the difference between the original stress and the sum of membrane and bending.

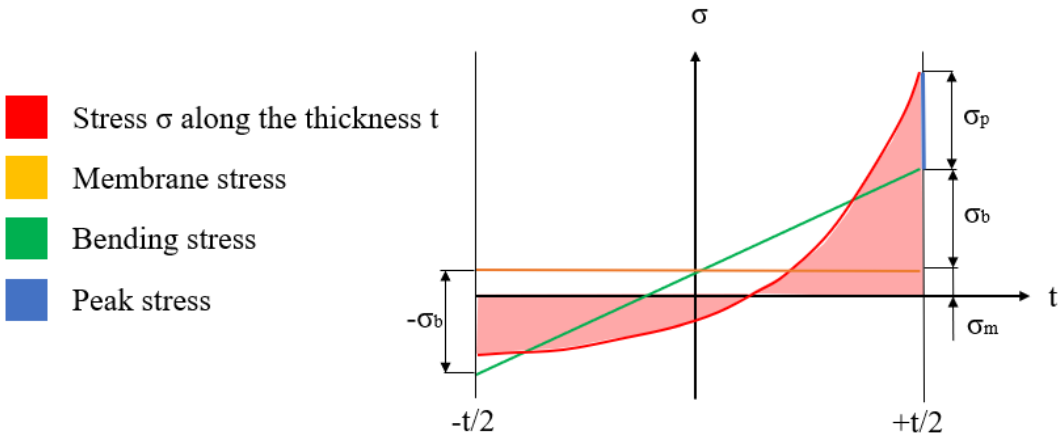

Figure 26: Linearization of a stress distribution along the thickness of a component with mechanical requirements.

Once presented the linearization of stresses, it is worth mentioning the way to apply this method in FEM models. The linearization of stresses is a methodology developed long time ago and based on the shell theory of continuous bodies. With this analytical procedure, the membrane and bending stresses are direct outputs of the assessment [46]. However, the FEM packages commonly offer the results as stress distribution computed with the Von-Mises or Tresca criteria. Therefore, a post-processing tool, usually integrated in the software, is needed to convert the results in linearized stresses. However, the method is not straightforward, being necessary the application of a method and the interpretation of the engineer.

The basic process to linearize the stresses obtained with FEM model can be resumed as follows:

- The complete stress distribution is studied to localize the zones with maximum average stresses or stress concentration points.
- In the zones considered as the most demanded or critical, the linearization paths are drafted between the mesh nodes to obtain the linearized stresses along them.
- Once the paths are drafted, it only remains the stress linearization. In the case of ANSYS Mechanical, the software implements the Stress Integration Method [45] to interpolate the stress between all the nodes found inside the drafted path and the stress is divided in membrane, bending and peak.

4.1.1 SMART Design Rules

For the study of the monotonic damage, the analysis will be based on the next hypothesis:

- The material has a linear-elastic behaviour.
- The material is isotropic, homogeneous and continuous.
- The strains and displacements are small.

And following the ITER SDC-IC, the designs rule considered will be:

- Membrane stress < Sm
- Membrane + Bending stress < 1.5 Sm
- Membrane + Bending stress + Peak stress < 2 Sm
- Primary + Peak + Secondary stress < 3.0 Sm

Being Sm the allowable stress limit of the materials, that is defined as the smaller value between 2/3 of the yield strength (Sy) and 1/3 of the tensile strength (Su).

Regarding the cyclic damage. The input for the analysis will come from the previous monotonic assessment, obtained with a FEM model. The rule for the **cyclic damage** will be:

- $\Delta\varepsilon < \Delta\varepsilon m$

Being $\Delta\varepsilon$ the maximum total strain range which is defined by Eq (1). $\Delta\varepsilon m$ is the maximum allowable total strain range which depends on the total number of cycles.

The total strain range is obtained by means of the next formula:

$$\Delta\varepsilon\ (\%) = 100\left(\Delta\sigma \cdot \left[\frac{2\ (1+\nu)}{3E}\right] + \left[\frac{\Delta\sigma}{K}\right]^{\frac{1}{m}}\right) \quad (1)$$

Being $\Delta\sigma$ the maximum stress range in the material (considering it as membrane + bending + peak). ν is the Poisson's ratio, E the Young's modulus, and K and m coefficients for the cyclic stress-strain relation.

Once the design rules that will be used to verify the structural integrity of the system have been presented, next section will discuss the FEM model created to study the system and the results obtained from it.

4.2 FEM Model

This section will present the Finite Element Method (FEM) model that has been created in ANSYS Mechanical for the structural assessment of the central stack of the SMART tokamak. First a description of the components

considered within the model will be shown. Next, the mesh and boundary conditions will be discussed.

As explained in the previous chapter, in the EM simulation we need the whole magnetic system to obtain the EM loads generated in the central stack conductors. Once they are obtained, for the structural assessment, only the conductors included in the central stack and the supporting elements are included.

The geometry included in the model is presented in the Figure 27. The elements considered are: TFC inner legs, central pole, PEEK insert, torque rings, torque arms and epoxy moulding. The rest of not structural components and details are neglected. Moreover, it is important to highlight that the central solenoid has also been neglected for this analysis. Its detailed verification is complex due to the helicoidal geometry of the conductor and is out of the scope of this project. It will be studied in future work projects. Moreover, it is considered, that the neglection in the simulation of the solenoid and its wrapping cylinder, is not relevant for the rest of the results, because they are not stiff elements that could change the structural behaviour of the complete system. Its weight (~200 kg) is only reacted by the pedestal that has a very conservative design and which analysis is not presented here neither for brevity.

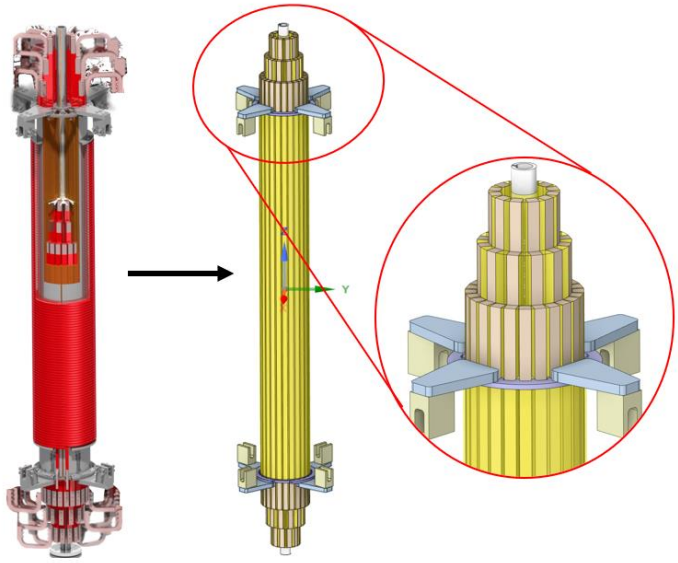

Figure 27: Geometry included in the structural FEM model.

The material properties for the copper and the SS316L is obtained from [47]. The properties of the aluminium 7075 T651 [48], the epoxy [33] and the PEEK [49] properties are obtained from its respective references. The properties are given for a temperature of 293K.

Table 5: Material properties at 293 K.

Material	Young's modulus (GPa)	Poisson's ratio	Density (kg/m^3)
AISI SS 316	200	0,296	7930
Aluminium 7075 T6	71.7	0.33	2810
Copper	117	0,33	8940
Epoxy	4	0.3	1180
PEEK	3.9	0.3	1320

Next, the boundary conditions of the model and the definition of the contact between all the elements will be explained. Due to the high number of components in the simulation, the interaction of them is highly influential in the results. First, a brief explanation of the boundary and contact types used will be given:

- **Bonded**: the nodes of the surfaces in contact are fixed, one to each other.
- **Frictionless**: the nodes of the surfaces in contact can slide within the surface plane and separate from it. However, the nodes cannot penetrate the surfaces.

- **Share Topology**: the meshes of element in contact are continuous. The nodes of faces in contact are shared. The geometry behaves as a block with the material properties of each different material on each component.

The boundary conditions and contacts of this model are summarized in the Figure 28 and explained below:

- **Central pole – Ground:** this condition is a frictionless support. It avoids the restriction of part of the torque by this condition, what would not be realistic, since in the reality the central pole will just be supported by the pedestal, but without being bolted.
- **Upper/Lower torque arms – Ground:** these conditions are frictionless supports again. They will restraint the torque, avoiding the reaction of part of the weight, that would not be real since the weight is completely reacted by the pedestal.
- **Epoxy – TFC bars, central pole, PEEK insert:** this condition is share topology. Since the epoxy can be considered as a glue that compact the whole system. This method is the most cost-effective computationally, since it does not include other restriction equations, just join mesh nodes from different components.
- **Epoxy – Torque rings:** this interaction is bonded. Instead of using share topology, a bonded boundary condition is included to have more control in the mesh of this important element with thin parts.
- **Torque rings – Torque arms**: for the same reason explained in the previous bullet point, this interaction is also bonded.

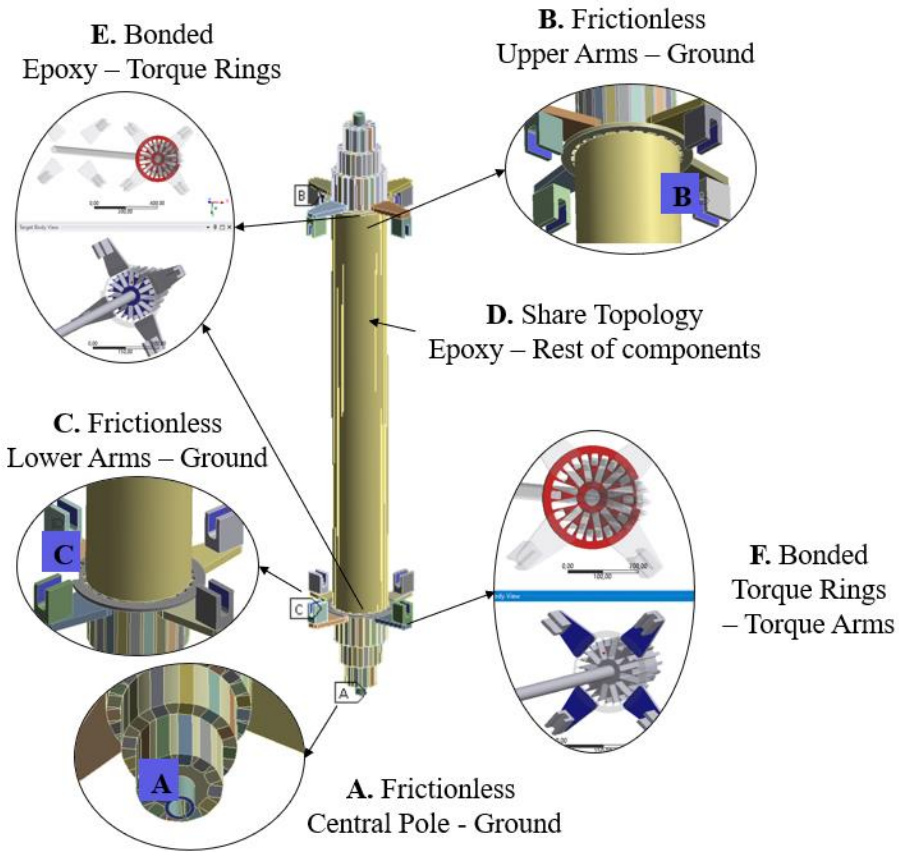

Figure 28: Boundary and contact arrangements of the model.

Finally, regarding the mesh of the model, it has 2.2 million nodes and 1.5 million elements. The general size of the mesh is 10 mm and all the elements, with except of the torque rings, are meshed with tetrahedrons to increase the ability of the software to mesh all the shapes and join them in the interfaces due to the share topology condition. Regarding the torque rings mesh, it has been refined with 3 mm hexahedrons and three elements along the thickness. In the contact zone of the torque ring with the epoxy blocks, the epoxy mesh has been refined up to 3 mm with an affected volume of 20 mm, to increase the coherence of the meshes in the contact areas. The mesh of the upper zone of the model is shown in Figure 29. The mesh of one of the torque rings is also shown in detail.

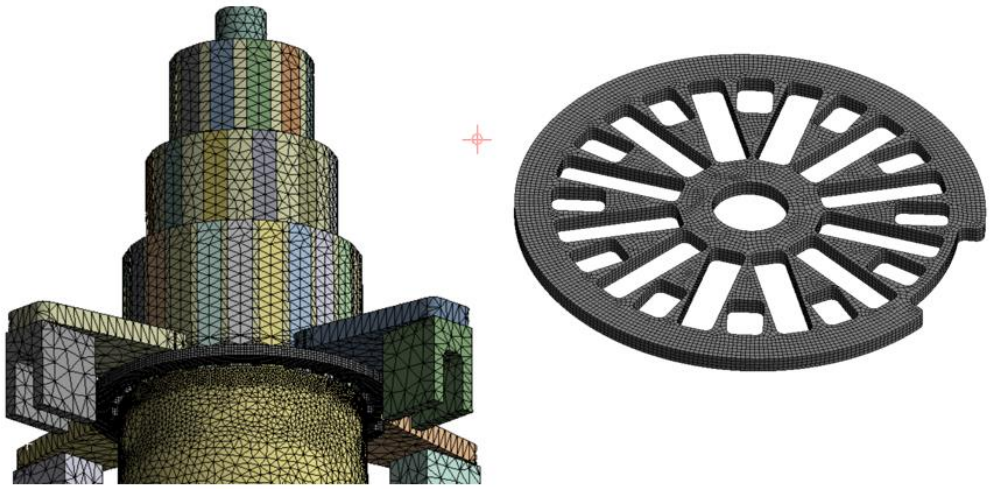

Figure 29: Mesh of the model in the upper zone and detail of one of the torque rings.

With this mesh, the results presented in the next section have been converged following the criteria of a lower error than 5 % between two consecutive iterations in all components except the torque rings. To converge the results in these rings, a sub-modelling technique has been applied, to refine only the mesh of the component in a separate model. This method will be presented in the next section.

4.3 Results

The results of the model will be presented in this section. These results will be compared with the design rules to check the structural integrity of all the components. First, the materials limits to define the rules are presented in the Table 6 (same sources than in Table 5).

Table 6: Design limits of the materials considered at 293 K.

Material	**Monotonic**			**cyclic**			
	Sy (MPa)	**Su (MPa)**	**Sm (MPa)**	**K (MPa)**	**m**	**Δεm (%) (N=1k)**	**Δεm (%) (N=100k)**
AISI SS 316	220	525	147	798.3	0.339	0.698	0.399
Aluminium 7075 T6	470	572	190	--	--	--	--
Copper	55	200	37	--	--	--	--
Epoxy	--	44	15	--	--	--	--
PEEK	95	103	32	--	--	--	--

For the monotonic damage, the Table 6 presents the yield strength (Sy), the tensile strength (Su) and the allowable stress (Sm). For the cyclic damage, the maximum deformation allowed for the material is presented for a given number of cycles. Moreover, the K and m factors needed for the assessment are included. Due to the data availability, only the SS316 component will be studied under cyclic damage. However, as will be seen next in the results, the most stressed components are those of SS316, therefore, the analysis is considered consistent. The total strain allowable is given for 1k cycles and for 100k cycles. This is because the results of the cyclic damage analysis will be obtained for two scenarios. First, for the design limit scenario (Bt=0.4 T and Ics=10 kA) and, second, for the baseline scenario of the SMART phase 2 operation (Bt=0.3 T and Ics=4 kA) when the load expected is much lower.

This differentiation is made because the design limit scenario is very critical, and it will be achieved only in certain and specific experiments where the maximum performance is expected. The rest of the experiments will be performed at the baseline performance, therefore, the life at this performance has to be much longer.

The following subsections will present the results of each component. For brevity, for the monotonic damage only the design limit scenario results are shown, since the of results of the baseline scenario will be always lower.

4.3.1 Copper bars

The Figure 30 shows the Von-Mises stress colour map of one set of 4 TFC inner legs. As can be seen, the stress is relatively low and distributed along the whole bars. In general, the stress is mainly compressive due to the In Plane Load (IPL) oriented to the centre of the column. However, near the torque rings, where the Out of Plane Load (OPL) is reacted, is where the maximum is located. In particular, the maximum appears in the outer bar that is the one between two set of three bars. In this zone a path has been drafted to linearize the stresses in membrane, peak and bending, as explained previously. Table 7 shows the stresses obtained along the path and the material limits. The green colour shows that the rules are fulfilled. As mentioned before, the cyclic damage is not studied because there is not data available of the fatigue curves, however, the stresses are relatively low and no special issue with fatigue is expected within this component.

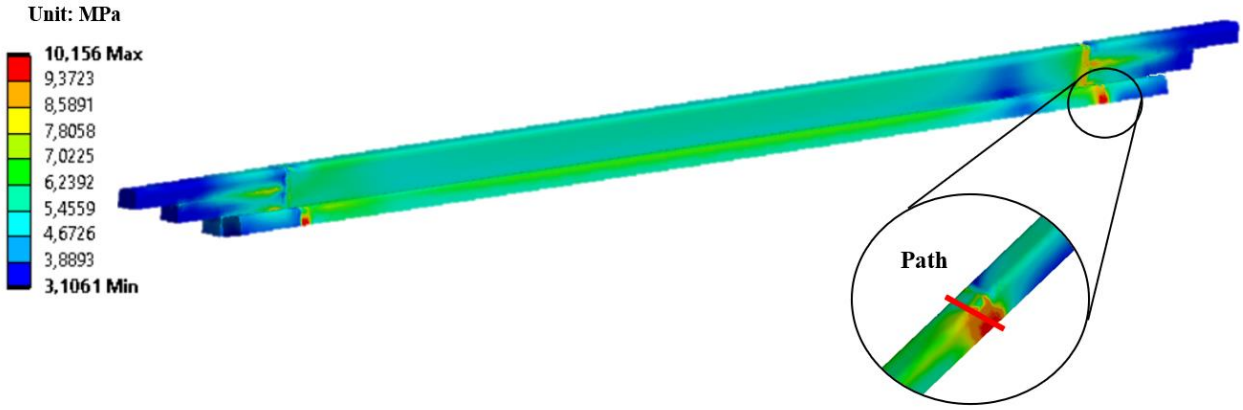

Figure 30: Von Mises stress colour map of the TFC inner legs for the design limit scenario.

Table 7: Monotonic damage verification of the copper bars.

Monotonic Copper bars	Membrane stress (MPa)	Membrane + Bending stress (MPa)	Membrane + Bending + Peak stress (MPa)
Rule	<Sm	<1.5 Sm	<2 Sm
Limit stress	37	55.5	74
Path P1	**3.9**	**5.1**	**10.2**

4.3.2 Central pole

The Figure 31 shows the Von-Mises stress colour map of the central pole. The stress in this component is generated by the weight of the system and by the TFC IPL, trying to compress the bar. Near the zone where the torque rings are attached, a path has been drafted to linearize the stresses. Table 8 shows the stresses obtained along the path and the material limits. The green colour shows that the rules are fulfilled. The cyclic damage is studied in this component (SS316L) for the design limit scenario (>1k cycles) and for the phase 2 baseline scenario (>200 k cycles) and the results are much lower than the limit values. Therefore, all the rules are fulfilled.

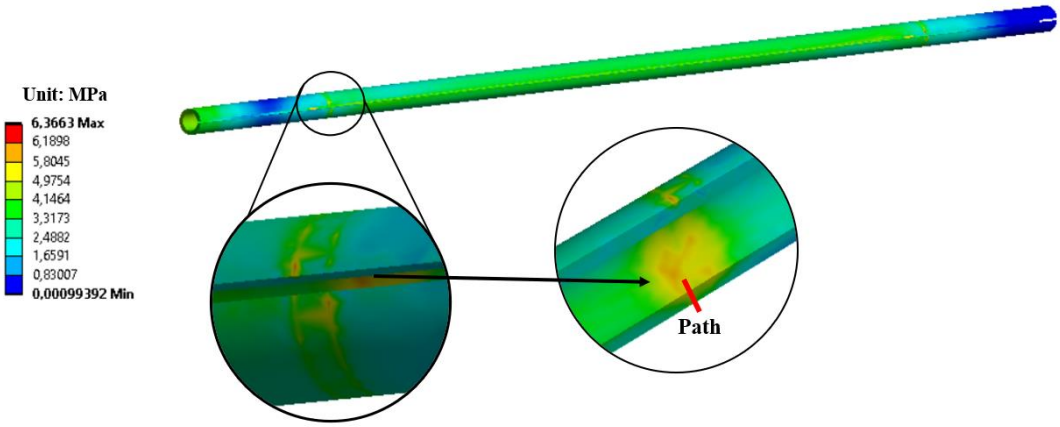

Figure 31: Von Mises stress colour map of the central pole for the design limit scenario.

Table 8: Monotonic and cyclic damage verification of the central pole.

Monotonic Central pole	Membrane stress (MPa)	Membrane + Bending stress (MPa)	Membrane + Bending + Peak stress (MPa)	Cyclic damage (%)	
Rule	<Sm	<1.5 Sm	<2 Sm	<$\Delta\varepsilon m$	
Limit stress	147	220.5	294	0.698 (N=1k)	0.250 (N=200k)
Path P1	**5.6**	**6.3**	**6.4**	**2.7×10^{-3}**	**9×10^{-4}**

4.3.3 Epoxy

The Figure 32 shows the Von-Mises stress colour map of the epoxy block. As can be appreciated, the stress in this component is in general very low. However, in the contact area with the torque rings, near the extremes, very localised areas have high stress. These peaks are mainly produced by the torque transmission from the copper bars to the torque rings. In one of these extremes, a path has been drafted to linearize the stresses and the Table 9 shows the results. As can be seen, all the values, except the last one, are below the limits. However, this is not considered as an important issue, because it would lead to a very localise yield in this area and a redistribution of the stress in the rest of the low loaded areas. Again, due to the lack of data, the cyclic damage is not studied, but it is not considered a problem in the general epoxy block because of the very low stress.

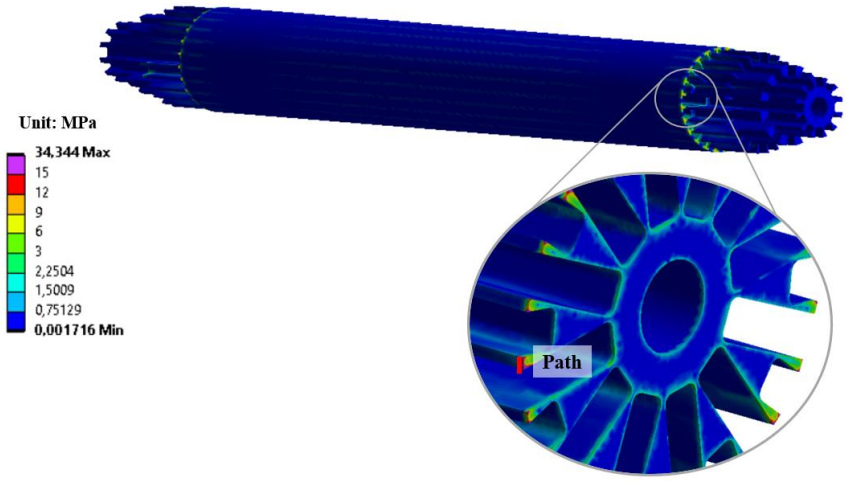

Figure 32: Von Mises stress colour map of the Epoxy moulding for the design limit scenario.

Table 9: Monotonic damage verification of the epoxy moulding.

Monotonic Epoxy	Membrane stress (MPa)	Membrane + Bending stress (MPa)	Membrane + Bending + Peak stress (MPa)
Rule	<Sm	<1.5 Sm	<2 Sm
Limit stress	15	22.5	30
Path P1	**9**	**20.7**	**34.4**

4.3.4 PEEK insert

The Figure 33 shows the Von-Mises stress colour map of the PEEK insert positioned in the central pole groove. The stresses are very low and almost negligible at the ends. A path is drafted in the middle of the component and the results along it are presented in Table 10. All the values are well below the limits. The fatigue is not studied for the lack of data, but it does not represent an issue.

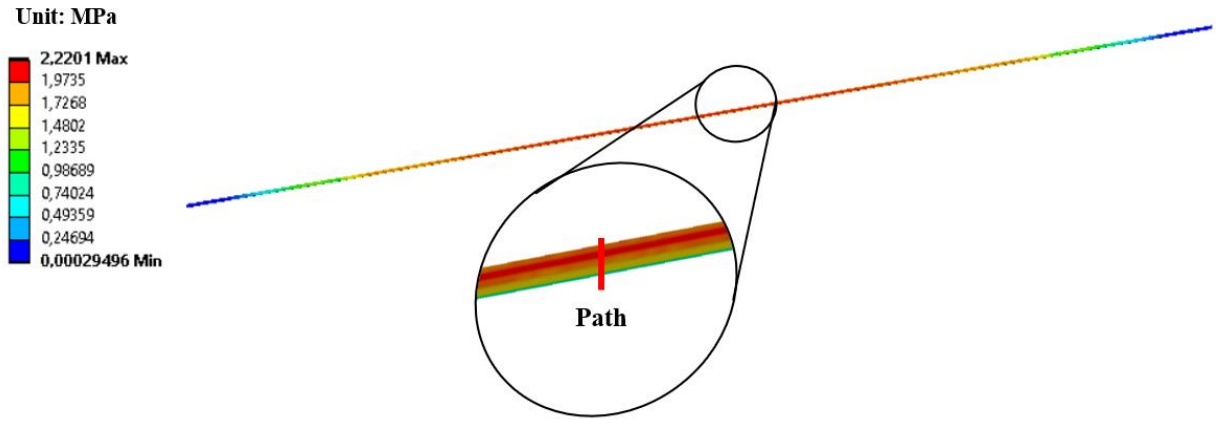

Figure 33: Von Mises stress colour map of the PEEK insert for the design limit scenario.

Table 10: Monotonic damage verification of the PEEK insert.

Monotonic PEEK insert	Membrane stress (MPa)	Membrane + Bending stress (MPa)	Membrane + Bending + Peak stress (MPa)
Rule	<Sm	<1.5 Sm	<2 Sm
Limit stress	32	48	64
Path P1	**1.5**	**2.1**	**2.2**

4.3.5 Torque Arms

The Figure 34 shows the Von-Mises stress colour map of the torque arms. As can be seen, the stresses are higher in the area where the arm is attached to the vacuum vessel ribs and where is attached to the torque rings. However, the stresses are relatively low. A path is included in the area where the arm touches the torque ring and the results are shown in the Table 11. All the values are well below the limits. The fatigue is not studied neither for the lack of data.

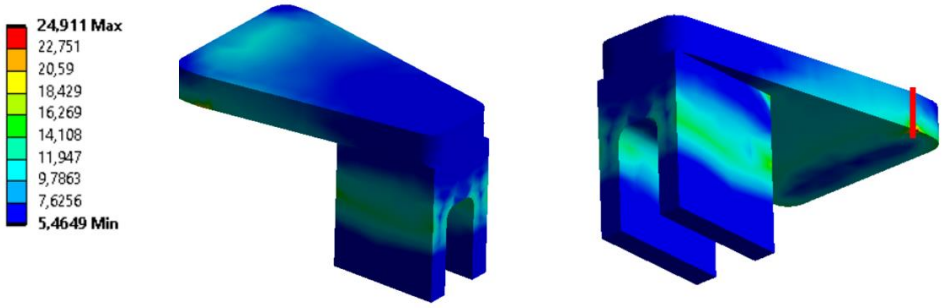

Figure 34: Von Mises stress colour map of the torque arms for the design limit scenario.

Table 11: Monotonic damage verification of the torque arms.

Monotonic Torque arms	Membrane stress (MPa)	Membrane + Bending stress (MPa)	Membrane + Bending + Peak stress (MPa)
Rule	<Sm	<1.5 Sm	<2 Sm
Limit stress	190	285	380
Path P1	**9.3**	**16.9**	**24.9**

4.3.6 Torque ring

Finally, the results in the torque rings are presented. In order to converge the results with the 5% criteria, a sub modelling technique has been applied. This technique is based on the analysis of just a part of a component in detail. In the cuts of the sub model, a boundary constraint is included. This constraint imports the results of the complete model to generate the same behaviour in the studied sub-volume. This technique allows a very cost-effective way of refining the mesh without high computational cost. The Figure 35 shows the mesh used in the sub-model, which has a general element size of 1.5 mm and, in the refined areas, of 0.7 mm. This figure shows also the results in the complete model and in the sub-model (converged). As can be seen, the torque rings suffer the highest stresses in the outer radii due to the reaction of the torque load. Near the outer groove of the ring, a path has been drafted to linearize the stresses in the area with the maximum stresses.

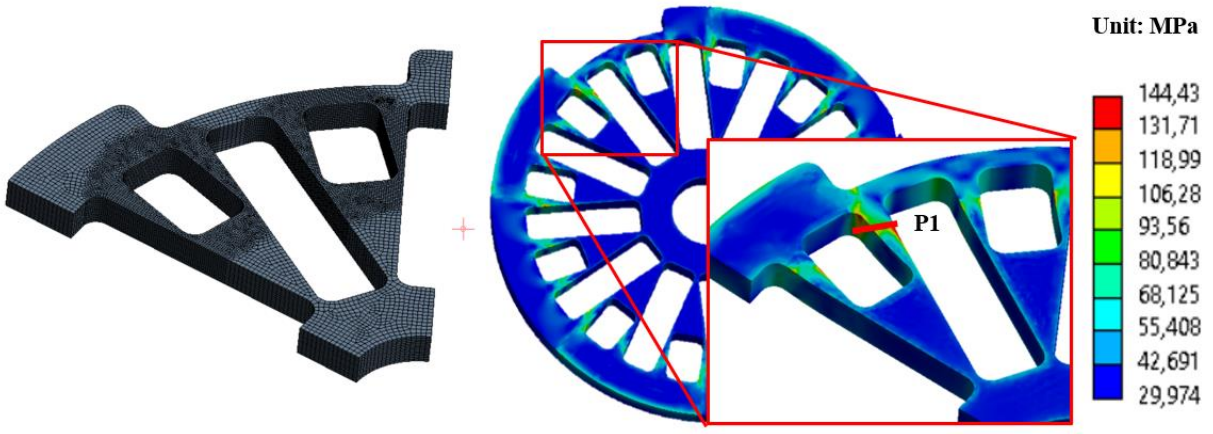

Figure 35: Mesh of the torque ring sub-model and Von Mises stress colour map of the torque ring for the design limit scenario.

Table 12: Monotonic and cyclic damage verification of the torque ring.

Monotonic Torque rings	Membrane stress (MPa)	Membrane + Bending stress (MPa)	Membrane + Bending + Peak stress (MPa)	Cyclic damage (%)	
Rule	<Sm	<1.5 Sm	<2 Sm	<$\Delta\varepsilon m$	
Limit stress	147	220.5	294	0.698 (N=1k)	0.250 (N=200 k)
Path P1	**48**	**120**	**144**	**0.204**	**0.025**

4.3.7 Displacements overview

Finally, once the structural verification of the system has been presented fulfilling all the rules, a general overview of the system displacement will be discussed. It will be just given to check that the system behaves as expected due to the load generated. The Figure 36 shows the directional deformation of the system in the Y axis (cylindrical coordinate system). As can be seen, the deformation meets almost perfectly with the deformation expected due to the torque generated by the OPL in the toroidal field coils. The maximum values in both directions are not exactly the same due to some types of asymmetries imposed by the irregularity of the load imported or the mesh, but they are minimum.

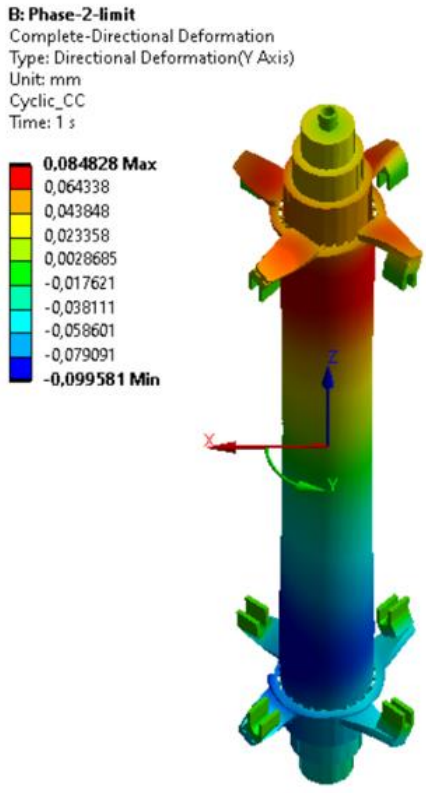

Figure 36: Displacement around the z axis of the central stack (y direction in a cylindrical coordinate system).

5 CONCLUSIONS AND FUTURE WORK

5.1 Conclusions

The design and analysis of the central stack for the SMART tokamak for its operation up to phase 2 has been presented. The ElectroMagnetic (EM) load generated in the central stack during the energization of the coils has been studied with a Finite Element Method model in the Software ANSYS Maxwell. The main loads generated are the In Plane Loads (IPL), due to the magnetic pressure in the coils and the Out of Plane Loads (OPL) in the Toroidal Field Coils (TFC). The OPL is generated by the interaction between the TFC electric current and the radial field at the ends of the solenoid. These loads obtained has been imported to another FEM model in ANSYS Mechanical to study the structural integrity of the system. The verification has been based on the ITER-SDC-IC code. The results can be summarised as follows:

- The stresses in the copper bars are well below the limits of the material, fulfilling all the rules. Due to the lack of data for the fatigue analysis it has not been performed, although the fatigue is not considered an issue in this component due to the low level of stress in them. Same conclusion is applied to the torque arms and the PEEK insert.
- The central pole has been studied against both monotonic and cyclic damage and all the rules are fulfilled again, since the component is very low stressed.
- The epoxy moulding has been studied only against monotonic damage, due to the lack of data for the fatigue study. This component is in general very low stressed, however, in the contact faces with the torque rings, some localised high stressed points appear. In these zones, one of the rules are not fulfilled, although it is not considered a structural issue because it is very localised and a redistribution of the load is expected in this area.
- The torque rings feature the highest level of stress due to the reaction of the torque load (OPL). A sub-modelling technique has been applied to converge the results and all of them are below the limits for both monotonic and cyclic damage.
- Regarding the complete Central Stack of the SMART tokamak, the minimum fatigue life, imposed by the machine operation requirements, is accomplished with big margins:
    - >>1k cycle at full machine operation
    - >>200k cycle at baseline scenario of phase 2

5.2 Future Work

There are several research lines as future work of this project. They are summarised as follows:

- Implement an experimental monitoring system to control in real time the structural behaviour of the tokamak (Methodology known as structural health monitoring [50]). This system can be coupled with numerical assessments like the one presented in this project to validate the results in a conservative way.

- Develop the design of the central stack for the operation of the SMART tokamak with phase 3 performance parameters. The much higher magnetic fields expected will lead to the increase of the load in correlation. The introduction of superconducting technology in the design might be an interesting line to increase the capabilities of the machine up to the state-of-the-art of the field.

REFERENCES

[1] R. Nave, "Nuclear Fusion," *HyperPhysics - Lecture Notes in Energy*, 2013. http://hyperphysics.phy-astr.gsu.edu/hbase/NucEne/fusion.html (accessed Apr. 24, 2021).

[2] BP, "Energy consumption by source, World," *Ourworldindata.Org*, 2020. https://ourworldindata.org/grapher/energy-consumption-by-source-and-region?time=earliest..latest (accessed Mar. 23, 2021).

[3] McKinsey, "Global Energy Perspective: Energy landscape," 2020. https://www.mckinsey.com/industries/oil-and-gas/our-insights/global-energy-perspective-2021?cid=other-eml-dre-mip-mck&hlkid=a774e1a8976d4a078406df70a8406fd5&hctky=1204056&hdpid=a9376fba-f827-4c5e-86f6-0dd5595597bc (accessed Mar. 22, 2021).

[4] DW, "Fearing Russian gas cutoff, Germans prepare for cold winter," 2022. https://www.dw.com/en/fearing-russian-gas-cutoff-germans-prepare-for-cold-winter/a-62412646 (accessed Aug. 27, 2022).

[5] H. Ritchie, "How long before we run out of fossil fuels? - Our World in Data," *Our World in Data*, 2017. https://ourworldindata.org/how-long-before-we-run-out-of-fossil-fuels (accessed Mar. 22, 2021).

[6] B. Gates, *How To Avoid a Climate Disaster: The Solutions We Have and the Breakthroughs We Need*, 1st ed. Random House USA, 2020.

[7] NationalgridESO, "Changes from FES 2019 to FES 2020," 2020. [Online]. Available: https://www.nationalgrideso.com/document/173791/download

[8] F. Rigas and P. Amyotte, "Myths and facts about hydrogen hazards," *Chem Eng Trans*, vol. 31, pp. 913–918, 2013, doi: 10.3303/CET1331153.

[9] NuScalePower, "Advanced Small Modular Reactors (SMRs) | Department of Energy," *Department of Energy*, 2021. https://www.energy.gov/ne/nuclear-reactor-technologies/small-modular-nuclear-reactors (accessed Mar. 23, 2021).

[10] A. Vallet, "Hydrodynamic modelling of the shock ignition scheme for inertial confinement fusion To cite this version : HAL Id : tel-01242131 DOCTEUR DE L ' UNIVERSITÉ DE BORDEAUX Modélisation hydrodynamique du schéma d ' allumage par choc pour la fusion par confineme," 2015.

[11] A. B. Zylstra *et al.*, "Burning plasma achieved in inertial fusion," *Nature*, vol. 601, no. 7894, pp. 542–548, Jan. 2022, doi: 10.1038/s41586-021-04281-w.

[12] N. Ida, *Engineering Electromagnetics*, vol. 15, no. 3. 1999. doi: 10.1109/MEI.1999.768566.

[13] N. A., "Learn About Motion Of A Charged Particle In A Magnetic Field," *Chegg Study*, 2021. https://www.chegg.com/learn/physics/introduction-to-physics/motion-of-a-charged-particle-in-a-magnetic-field (accessed Apr. 25, 2021).

[14] A. Milantiev and V. Temko, *Plasma Physics*. URSS editorial, 1987.

[15] M. Kikuchi, K. Lackner, and M. Quang, "Fusion Physics," *Iaea*, pp. 24–26, 2012.

[16] J. Wesson, *Tokamaks* , 4th ed. Oxford ; Oxford University Press, 2011.

[17] V. Erckmann *et al.*, "Electron cyclotron heating for W7-X: Physics and technology," *Fusion Science and Technology*, vol. 52, no. 2, pp. 291–312, 2007, doi: 10.13182/FST07-A1508.

[18] D. Battaglia, "Introduction to Tokamaks and Spherical Tokamaks," 2020.

[19] U. S. D. of Energy, "Project Execution Plan for the U.S. Contributions to ITER," 2017.

[20] J. A. Reusch *et al.*, "Non-inductively driven tokamak plasmas at near-unity β t in the P egasus toroidal experiment," *Phys Plasmas*, vol. 25, no. 5, 2018, doi: 10.1063/1.5017966.

[21] A. E. Costley, J. Hugill, and P. F. Buxton, "On the power and size of tokamak fusion pilot plants and reactors," *Nuclear Fusion*, vol. 55, no. 3, 2015, doi: 10.1088/0029-5515/55/3/033001.

[22] J. E. Menard *et al.*, "Fusion pilot plant performance and the role of a sustained high power density tokamak," *Nuclear Fusion*, vol. 62, no. 3, Mar. 2022, doi: 10.1088/1741-4326/ac49aa.

[23] M. Gryaznevich, "Progress Towards Compact Fusion Reactor," no. May, 2015.

[24] S. J. Doyle *et al.*, "Single and double null equilibria in the SMART Tokamak," *Plasma Research Express*, vol. 3, no. 4, Dec. 2021, doi: 10.1088/2516-1067/ac2a0e.

[25] N. A., "What is Lorentz's strength?," *imamagnets*, 2021. https://www.imamagnets.com/en/blog/what-is-lorentz-strength/ (accessed May 02, 2021).

[26] M. Agredano Torres, "Coils and power supply design for the SMall Aspect Ratio Tokamak (SMART) of the University of Seville," University of Seville, 2020.

[27] C. Neumeyer *et al.*, "NSTX TF joint failure and re-design," in *Proceedings - Symposium on Fusion Engineering*, 2003, pp. 35–38. doi: 10.1109/fusion.2003.1425872.

[28] V. Thompson, G. Voss, I. Katramados, and M. Harte, "MAST Upgrade centre column design and analysis," in *Fusion Engineering and Design*, Oct. 2011, vol. 86, no. 6–8, pp. 1398–1401. doi: 10.1016/j.fusengdes.2011.03.112.

[29] V. B. Minaev *et al.*, "Magnetic System for the Upgraded Spherical Tokamak Globus-M2."

[30] G. S. Kurskiev *et al.*, "Tenfold increase in the fusion triple product caused by doubling of toroidal magnetic field in the spherical tokamak Globus-M2," *Nuclear Fusion*, vol. 61, no. 6, Jun. 2021, doi: 10.1088/1741-4326/abe08c.

[31] Luvata, "Luvata - the most diverse and innovative metals manufacturing group in the world." https://www.luvata.com/ (accessed Sep. 09, 2022).

[32] Royal Diamond, "TUFQUIN TFT (UL) - Royal Diamond your insulation partner." https://royal-insulation.com/tufquin-tft-ul (accessed Sep. 09, 2022).

[33] Sicomin, "SR 1720 / SD 7840 technical datasheet." Accessed: Sep. 09, 2022. [Online]. Available: http://sicomin.com/datasheets/product-pdf99.pdf

[34] P. H. Titus, H. Becker, D. Gwinn, K. Rettman, and P. Stahle, "Failure analysis and design improvement of the alcator C-mod toroidal field coil sliding joint," in *Proceedings - Symposium on Fusion Engineering*, 1999, pp. 427–432. doi: 10.1109/fusion.1999.849871.

[35] B. K. Huang, M. Mason, A. McFarland, P. Noonan, J. S. H. Ross, and A. Sykes, "Joint testing of the 3 Tesla ST40 spherical tokamak toroidal field coil test assembly," *Fusion Engineering and Design*, vol. 124, pp. 64–68, Nov. 2017, doi: 10.1016/j.fusengdes.2017.04.115.

[36] A. Zolfaghari, T. Willard, and M. Smith, "Coupled multiphysics analysis of the TF coil structure in the NSTX upgrade," 2011. doi: 10.1109/SOFE.2011.6052349.

[37] MGC, "MGC - Make Good Composites", Accessed: Sep. 09, 2022. [Online]. Available: https://www.mgcomposites.es/

[38] Ansys, "ANSYS Maxwell V16," 2013.

[39] S. J. Doyle *et al.*, "Magnetic equilibrium design for the SMART tokamak," *Fusion Engineering and Design*, vol. 171, Oct. 2021, doi: 10.1016/j.fusengdes.2021.112706.

[40] A. Mancini *et al.*, "Mechanical and electromagnetic design of the vacuum vessel of the SMART tokamak," *Fusion Engineering and Design*, vol. 171, Oct. 2021, doi: 10.1016/j.fusengdes.2021.112542.

[41] ANSYS, *ANSYS Mechanical APDL Technology Demonstration Guide*, vol. 3304, no. October. 2012.

[42] G. Sannazzaro *et al.*, "Development of design Criteria for ITER In-vessel Components," *Fusion Engineering and Design*, vol. 88, no. 9–10, pp. 2138–2141, 2013, doi: 10.1016/j.fusengdes.2013.01.019.

[43] D. de Meis, "Structural design codes for nuclear components," 2016.

[44] V. Barabash, *ITER Structural Design Criteria - In-vessel Components*. 2012. [Online]. Available: G 74 MA 8 01-05-28 W 0.2

[45] N. A., "Stress Linearization in Ansys Workbench compatible with ASME BPVC," *Simutech*. https://simutechgroup.com/stress-linearization-in-ansys-workbench-compatible-with-asme-bpvc-2/ (accessed Apr. 25, 2021).

[46] G. C. Slagis, "ASME section III design-by-analysis criteria concepts and stress limits," *Journal of Pressure Vessel Technology, Transactions of the ASME*, vol. 128, no. 1, pp. 25–32, 2006, doi: 10.1115/1.2140797.

[47] V. Barabash, *Structural Design Criteria for In-vessel Componentes - Appendix A , Materials Design Limit Data*. 2013. [Online]. Available: G 74 MA 8 01-05-28 W 0.2

[48] MatWeb, "Aluminum 7075-T6; 7075-T651", Accessed: Sep. 09, 2022. [Online]. Available: https://www.matweb.com/search/DataSheet.aspx?MatGUID=4f19a42be94546b686bbf43f79c51b7d&ckck=1

[49] Dielectric MFG, "Material Properties of Thermoplastic PEEK - Polyetheretherketone", Accessed: Sep. 09, 2022. [Online]. Available: https://dielectricmfg.com/knowledge-base/peek/

[50] A. M. Nazar, P. Jiao, Q. Zhang, K. J. I. Egbe, and A. H. Alavi, "A New Structural Health Monitoring Approach Based on Smartphone Measurements of Magnetic Field Intensity," *IEEE Instrum Meas Mag*, vol. 24, no. 4, pp. 49–58, Jun. 2021, doi: 10.1109/MIM.2021.9448251.